



Government of **Western Australia**
Department of **Mines and Petroleum**

RECORD 2009/13

AGE CONSTRAINTS AND DEFORMATION HISTORY OF THE SHAG HILL MYLONITES, WESTERN MUSGRAVES

by
Michael Belperio



Geological Survey of
Western Australia



Age constraints and deformation history of the Shag Hill mylonites, western Musgraves

Michael Belperio

Continental Evolution Research Group
School of Earth and Environmental Sciences
The University of Adelaide



Date: 25th day of October, 2006

Notice to the reader

This Record is one of a series of BSc. Hons theses researched, written and compiled by students from the Centre of Tectonics, Resources and Exploration (TRaX), University of Adelaide, through an ongoing collaborative project between the Geological Survey of Western Australia (GSWA) and the University of Adelaide. Although GSWA has provided field and laboratory support for this project, the scientific content of each Record, and the drafting of figures, has been the responsibility of the authors. No editing has been undertaken by GSWA.

All work carried out in the west Musgrave region is done so within the framework of an ongoing collaborative project involving GSWA, the Traditional Owners of the region and the Ngaanyatjarra Council. The considerable efforts of the Traditional Owners and of the Ngaanyatjarra Council in facilitating this work is gratefully acknowledged.

Table of Contents

Table of Contents	1
Abstract	2
1. Introduction	4
2. Regional geology	5
3. Field relationships	10
3.1. Lithology	10
3.2. Structure	12
4. Mafic petrology and geochemistry	14
5. Geochronology	19
5.1. Analytical procedure	19
5.2. Sample descriptions	20
5.2.1. 155710: felsic dyke	20
5.2.2. 155712 & 155750: mylonitic shear zones	21
5.3. Results	21
5.3.1. 155710: felsic dyke	22
5.3.2. 155712: NE-SW mylonitic shear zone	23
5.3.3. 155750: E-W mylonitic shear zone	24
5.4. Standard errors	25
5.5. Discussion	26
6. Timing of deformation	27
7. Microanalysis	29
7.1. Optical microstructural analysis	29
7.1.1. Foliated granite; sample 155747	29
7.1.2. Ultramylonite; samples 155705, 155706	29
7.1.3. Mylonite; samples 155750, 155712	30
7.1.4. L-tectonite; sample 155751	31
7.2. Electron backscatter diffraction analysis	32
7.2.1. Methodology	32
7.2.2. Analysis	33
7.2.3. Results	36
7.3. Discussion	39
7.3.1. Foliated granite	40
7.3.2. Ultramylonite	41
7.3.3. Mylonite	41
7.3.4. L-tectonite	43
8. Conclusions	44
Acknowledgements	45
References	46

Age constraints and deformation history of the Shag Hill mylonites, western Musgraves

Michael Belperio

Continental Evolution Research Group
School of Earth and Environmental Sciences
University of Adelaide

Abstract

Multiple generations of crosscutting shear zones cut through the gneissic Wankanki Supersuite granite of the western Musgrave Block. SHRIMP U-Pb dating of zircons, both from mylonitic shear zones within the gneiss and from a felsic dyke with an earlier high strain fabric, reveal no evidence for either of these two, separate, deformational events. The geochronology does, however, identify crystallisation ages of c.1304 Ma for the Wankanki Supersuite granite, and also a record of metamorphism at c.1195 Ma, which predates the shear zone deformation. The c.1195 Ma age of metamorphism is associated with the terrain-scale Musgravian Orogeny (c.1300-1100 Ma), and is linked to the widespread gneissic foliation in the Wankanki Supersuite granite. All mylonites cut mafic dykes chemically correlated with the c.820 Ma Amata dyke swarm, constraining shear zone deformation to <820 Ma. Structural style and kinematics are consistent with these mylonites being formed during the Petermann Orogeny.

All shear zones possess almost exclusively south side up kinematics in outcrop and in thin section, while the interpretation of quartz crystallographic orientation data suggests a separate, later north side up deformational shear sense unobserved in mesoscale observations. Microstructural and mineralogical evidence both indicate at least two stages of deformation within both the mylonitic and ultramylonitic shear zones, with the later operat-

ing at lower temperature conditions than the earlier. The difference in deformational grade is interpreted to represent exhumation of the shear zones synchronous with their associated deformation during the Petermann Orogeny. Optical microscopy and electron backscatter diffraction analysis has revealed heterogeneities within the mylonitic deformation, with partitioning of coaxial and non-coaxial deformation within larger high strain zones resulting in domains of L-tectonic and S-L tectonic high strain zones.

Keywords: Musgrave Block, Petermann Orogeny, SHRIMP, EBSD, Quartz, Strain

1. Introduction

The Musgrave Block preserves evidence of an extensive history of multiple large-scale deformation and metamorphic events. The Neoproterozoic Petermann Orogeny was a widespread, and high grade event, which has controlled the outcrop pattern in the Musgrave Block, and which has also overprinted much of the evidence of earlier deformational events (Camacho and Fanning, 1995). As a result, the investigation of the structural, metamorphic and geochronological aspects of the earlier deformational periods is often complicated by conflicting and overprinted evidence.

A series of crosscutting shear zones are located in a small hill, Shag Hill, in the western portion of the Musgrave Block (Fig. 1). The field site is located south of the E-W trending Mann-Hinckley Fault, which formed a major shear boundary during the Petermann Orogeny, juxtaposing terrains that experienced Neoproterozoic metamorphism at different crustal depths (Camacho and Fanning, 1995). To the south of the Mann-Hinckley Fault, Petermann-aged deformation was not as pervasive as north of the shear zone. In this study, the different shear zone generations of Shag Hill are investigated in an attempt to provide a chronologic and strain framework for the observed deformation.

This study presents the field structural relationships of the Shag Hill shear zones. Geochemical analysis is used to link deformed mafic outcrops to known igneous suites in order to constrain the relative timing of mylonitic deformation, while U-Pb zircon Sensitive High Resolution Ion Microprobe (SHRIMP) analyses is used in an attempt to provide direct chronological data for specific deformational features. In addition, optical microscopic strain analysis, in conjunction with Electron Back Scatter Diffraction (EBSD)

analysis, are used in an attempt to characterise the strain associated with the different shear zone events, and to link microscopic strain features with the macroscopic features observed in outcrop.

2. Regional geology

The Musgrave Block is an approximately 120,000 km², latitudinally trending, Meso-Neoproterozoic mobile belt within central Australia (Fig. 1). The region is bounded to the north and south by Neoproterozoic sedimentary basins (the Amadeus and Officer basins, respectively), which may be related to crustal extension during the early stages of the break up of the supercontinent Rodinia (White et al., 1999).

The earliest regional geological descriptions of the area were undertaken by Forman (1965; 1972) and also Sprigg and Wilson (1959). Early geochemical and geochronological studies were undertaken by Gray (1977, 1978). More recent publications have focused on the study of orogenic geochronology (Camacho et al., 1997; Camacho and Fanning, 1995; White et al., 1999), orogenic pressure-temperature histories (Maboko et al., 1991; Scrimgeour and Close, 1999), isotope based provenance (Wade et al., 2005), and studies into the igneous aspects of the region (Glikson et al., 1996; Wade et al., 2006).

Early interpretations of the eastern Musgrave Block (Collerson et al., 1972; Thomson, 1976) produced three main subdivisions based upon structural and metamorphic differences – the Central, Northern and Southern terrains (dominated by granulite, amphibolite and transitional amphibolite-granulite facies, respectively). Further interpretations (Camacho and Fanning, 1995) regarded the Central and Southern terrains to be metamor-

phically and isotopically indistinguishable, except for the more extensive hydration in the Southern terrain.

The currently used divisions regarding the Eastern Musgraves involve the amphibolite facies Mulga Park Subdomain, and the granulite to transitional-granulite facies Fregon Subdomain (Major and Conor, 1993). The former essentially encompasses the geology of Collerson's (1972) Northern terrain (i.e. the amphibolite rocks structurally below the Woodroffe Thrust), while the latter includes the higher-grade geology of the Central and Southern terrains (i.e. above the Woodroffe Thrust; Camacho and Fanning, 1995). Despite the difference in metamorphic grade between the two subdomains, the same gneiss precursor age (~1550 Ma) and the same structural and magmatic events in the two subdomains indicate that the two represent the same structural block (Camacho and Fanning, 1995). The difference in metamorphic grade represents the different crustal depth of the two, originally singular, blocks, which were juxtaposed by the Woodroffe Thrust during the Petermann Orogeny (Camacho and Fanning, 1995).

The dominant rocks of the Musgrave Block are 1600-1300 Ma ortho- and paragneisses and 1250-1150 Ma granites (Gray, 1978; Myers et al., 1996; White et al., 1999). Some orthogneisses have been interpreted to have volcanic precursors with two discrete ages – c.1550 and c.1330 Ma (Gray, 1977; Gray, 1978). A large felsic magmatic event intruded between 1296-1324 Ma, which was contemporaneous with the earliest metamorphism/deformation event of the region (D_1) at c.1315 Ma (White et al., 1999). This event was previously interpreted to be synchronous with the D_2 event at c.1200 Ma, based upon poorly constrained Rb-Sr whole-rock isochrons (Gray, 1978). D_2 has since been defined as a separate, terrain-scale, orogenesis known as the Musgravian Orogeny.

This high-grade event produced zircon overgrowths yielding c.1200 Ma U-Pb ages (White et al., 1999), and metamorphic conditions in excess of 750°C and 5±1kbar (Clarke et al., 1995). This upper amphibolite to granulite facies metamorphism is associated with OPX-garnet bearing felsic gneisses and rare sillimanite-garnet bearing metapelitic gneisses (Clarke et al., 1995) and substantial crustal thickening between ~1200-1150 Ma (Camacho and Fanning, 1995; Myers et al., 1996).

The c.1300 and c.1200 Ma magmatic/deformation events are correlated with similar events in the Albany-Fraser Orogen of southwestern Australia (Clark et al., 2000), and the Windmill Islands and Bunger Hills of east Antarctica (White et al., 1999). Together, these terrains, and their contemporaneous deformations, are interpreted as a protracted Grenvillian orogenic event caused by the accretion of various cratons (North Australian Craton, South Australian Craton, Mawson Craton) during the assembly of Rodinia, ~1300-1000 Ma (Betts et al., 2002; Clark et al., 2000; Giles et al., 2004; White et al., 1999).

D₂ was followed by decompression and a further felsic magmatic event. The uplift and erosion was restricted to discrete portions of the Fregon terrain, located in the central and eastern parts of the Musgrave Block, producing high-grade decompression textures in metapelitic gneisses (Maboko et al., 1991; White et al., 1999). The igneous age of fine-grained and rapakivi granitoids (Pitjantjatjara Supersuite granite of the Western Australian and Northern Territory Geological Surveys, Bodorkos et al., 2006; Edgoose et al., 2004)) is constrained at c.1188 Ma (Sun et al., 1996). This intrusion is thought to be related to the post-D₂ uplift, although no direct evidence is currently available (White et al., 1999).

The Giles Complex, a major suite of mafic/ultramafic layered sills, intruded following D_2 , at around c.1080 Ma (Glikson et al., 1995; Glikson et al., 1996; Sun et al., 1996). A range of post- S_2 mafic dykes, some of which may represent feeder dykes to the Giles Complex, also intruded c.1073 Ma (Glikson et al., 1995; Sun et al., 1996), while the mafic and felsic volcanics of the Tollu Group have an U-Pb SHRIMP age of c.1078 Ma, and thus are thought to have a genetic relationship with the Giles Complex (Sun et al., 1996). Pressure estimates associated with the Giles intrusions range from 6-12kbar, with the wide variation attributed to the emplacement of bodies at different crustal depths and/or to partial re-equilibration during metamorphism (Ballhaus and Glikson, 1995; Glikson et al., 1995).

The next major phase of metamorphism, D_3 , attained granulite facies at c.1060 Ma (Sun et al., 1996), and is responsible for the southeasterly trending, near vertical foliation that is pervasive through much of the western Musgraves. The deformational period resulted in a wide range of structural features, with mesoscopic F_3 folds ranging from tight to isoclinal, and upright to reclined (Glikson et al., 1995; White et al., 1999) and a steep southerly-dipping mylonitic axial planar fabric (Glikson et al., 1996).

Post-dating the D_3 deformation are the intrusion of two different mafic dyke sets, (type C and type B of Glikson et al, 1996), at c.1000 and c.800 Ma respectively (Glikson et al., 1995; Glikson et al., 1996; Sun et al., 1996). Type B dykes can broadly be correlated with the Amata and Gairdner swarms of the central Musgraves and Gawler Craton (Glikson et al., 1996), and when cut by high-grade mylonitic shear zones, give a maximum age for the associated D_4 event.

Clarke (1992) distinguished three separate shear zone forming events (D₄-D₆), with a forth shear zone event (D₇) reported by Glikson et al. (1995). D₄ shear zones are amphibolite facies, E-W trending mylonitic-ultramylonitic zones, 10-100s m wide, reflecting dominantly reverse movement, and involving displacements estimated up to 100m, along a SE-orientated transport direction. These D₄ shear zones define the boundaries of the terrain-scale, E-W trending, Hinckley Fault (Glikson et al., 1995). The D₅ ultramylonitic greenschist facies shear zones offset D₄. D₅ shear zones dip steeply to the east, with a SW directed transport direction, again inferred to have involved 100s of metres of, dominantly reverse, movement (Clarke et al., 1995; Glikson et al., 1995). D₆ is defined by deformation across a larger-scale zone (150-500 m wide), involving southerly dipping, steeply plunging mineral stretching lineations and extensive pseudotachylite development. This D₆ shear zone event is related to the terrain-scale Woodroffe Thrust, across which movement during the c.550 Ma Petermann Orogeny resulted in: (1) northward displacement of the Musgrave Block over the Proterozoic-Palaeozoic Amadeus Basin; (2) the dissection of deep crustal blocks in the central and eastern Musgraves; and (3) the subsequent positioning of much of the present day outcrops/exposure (Camacho and Fanning, 1995; Clarke et al., 1995; Glikson et al., 1995). The post-Petermann D₇ shear zones are poorly exposed biotite/muscovite-bearing retrograde shear zones, which dip north and possess a reverse sense of movement (Glikson et al., 1995). Clarke et al. (1995) suggests the probability that D₄-D₇ represent a single evolving orogenic event.

3. Field relationships

Field work for this study was undertaken at Shag Hill, an approximately 400×200m patch of outcrop nestled between the Bell Rock Range, and the Hinckley Ranges, in Western Australia, roughly 20km from the Western Australia, South Australia and Northern Territory borders (Fig. 1). The detailed observations at Shag Hill reflect a microcosm of the protracted structural and deformational history of the Musgrave Block. Field relationships identify at least four separate deformational periods, represented by: (1) pervasive gneissic foliation; (2) a high strain fabric within a felsic dyke; (3) relatively high-grade mylonites; and (4) a relatively lower grade ultramylonite. The lithological and structural features of Shag Hill are shown in Figure 2.

3.1. Lithology

Shag Hill possesses a fairly simple lithological framework. The near exclusive lithology is a moderately foliated granitic gneiss (the Wankanki Supersuite granite, Howard et al., 2006). This unit is mineralogically homogeneous, with the foliation defined primarily by elongated K-feldspar with minor biotite and quartz, but shows considerable heterogeneity in terms of structure and foliation. The occurrence of the Wankanki Supersuite granites delineates a large terrain in the western Musgraves around Mt West and Michael Hills, and continues westward into the Blackstone region, where it is only found south of the Mann-Hinckley Fault (Howard et al., 2006). The Wankanki Supersuite granites encompass the 1330-1300 Ma felsic orthogneisses of White et al. (1999), and for which the

Geological Survey of Western Australia have detailed SHRIMP U-Pb zircon crystallisation ages ranging from 1300-1290 Ma (GSWA, unpublished data)

A number of discrete felsic and mafic igneous bodies cut across the felsic gneiss and its associated foliation. Felsic dykes, generally <2m wide, run in a NW-SE orientation, and in some cases are offset up to 40m by mylonitic shear zones. The similar orientation of a number of felsic dykes implies a single genetic event, however, the possibility exists that the different dykes are just displaced sections of a single dyke that has been split up by various mylonitic events (Fig. 2).

The mafic intrusions of the area exhibit a range of thicknesses, orientations, petrology and morphology, and some may actually form tectonic pods, rather than original igneous intrusions (discussed below). Dolerite dykes exist as either <2m wide NE-SW trending planar intrusions, or as <5m wide, roughly NW-SE trending bodies. Thicker mafic bodies (up to 10m wide) trend roughly E-W and have no intrusion-related crosscutting relationships to the host rock. These thicker bodies are medium to coarse-grained gabbros with small veinlets (or 'sweats'; 5-10cm long) of coarse-grained quartz and feldspar throughout. Where directly associated with shearing, the felsic veinlets transform from their natural, irregular shape, to straight sheared bands, which are elongate in the direction of shearing. This bimodal, mafic/felsic petrology is consistent with the large volume Hinckley Range Gabbro (HRG) intrusion (Glikson et al., 1996), and these gabbro bodies are hereafter referred to as such.

3.2. Structure

The pervasive gneissic foliation dips steeply to the NW or SE (Fig. 3), and varies in intensity from moderate to strong. The increase in foliation intensity within the gneiss, and also the variations in orientation (eg the gneissic foliation outliers in Fig. 3) often reflect the proximity to younger structural features (eg mylonitic zones). In some cases, the gneissic foliation transposes into the mylonitic foliation over 10s of metres. Isolated enigmatic patches of strong or atypically orientated foliation may reflect a concealed or eroded higher-grade structural feature.

Multiple generations of shear zones cut across the granitic gneiss, and are characterised by: (1) foliations and mineral elongation lineations plunging steeply to the north-northwest (Fig. 3); (2) south side up kinematics both on the macro- and micro-scale; and (3) cutting (and possibly displacement) of the mafic and felsic dykes.

The oldest generation of shear zones are mylonitic zones, 1-10m wide, curving from NE-SW (in the east) to NW-SE (in the west). In the southeast of the hill, continuous >100m long mylonite zones curve around from a NE-SW strike to an E-W orientation (Fig. 2).

A NW-SE trending felsic dyke (sample 155710) is truncated to the south by one of the aforementioned mylonites. This contains a sub-mylonitic foliation running sub

-parallel to the dyke margins. Not only is the orientation of this high-grade fabric different from both the widespread gneissic foliation and the foliations within the surrounding shear zones, the foliation of the granitic gneiss host rock is transposed into the dyke over a range of approximately 15-20m.

This dyke/shear zone is truncated to the north by a younger shear zone, which also cuts the felsic and mafic dykes, and the aforementioned mylonitic zones. This ultramylonitic zone is thin (1-5m thick), planar, and trends E-W for approximately 300m. The abundance of epidote within the ultramylonite, which exists as fracture fill both on the macro- and micro-scale, limits this shear zone to lower amphibolite to greenschist facies, however the abundance of mm- to cm-scale pseudotachylite veins indicate a higher strain rate than within the mylonitic zones.

In addition to the foliation/lineation dominated (i.e. mylonitic) granitic gneiss, discrete portions of the terrain also consist of lineation-dominated tectonites ('L-tectonites'; Fig. 2), with steep mineral stretching lineations parallel to the lineations in the mylonitic zones. The L-tectonite zones are discrete patches that are confined between two or more mylonitic zones, suggesting partitioning of strain in the shear zones into coaxial (L-tectonic) and non-coaxial (mylonitic) domains. This implies that the shear zones are not distributed as multiple discrete (parallel) mylonitic zones <10m wide, but are much wider, singular, zones that encompass the transitions through mylonites and L-tectonites. The evolution between coaxial and non-coaxial deformation is investigated later in this study (section 7).

Slivers of mafic material, both dolerite and HRG on the cm- and m-scale, are observed within the L-tectonites and the mylonites. Where these slivers correspond to the edge of an outcrop (e.g. Fig. 4), the sliver extends, parallel to the lineation, into the ground. In the case of the L-tectonite in Figure 4, the extension in the dolerite sliver is in excess of 2m. The inference is that small pieces of dolerite and HRG, incorporated in the shear zone, have been stretched out parallel to the mineral lineation during the associated

deformation. Lamination-rimmed slivers of dolerite on the cm-scale are quite commonly embedded within the mylonitic gneiss or L-tectonite, however metre-sized outcrops of HRG also have the same relationship to the mylonites (e.g. samples 155724 and 155725; Fig. 2), again with the inference that these blocks have been stretched, during the mylonitic deformation, along the mineral lineation (Fig. 5). No estimates are placed on exactly what depth these slivers/blocks originate from, or how far they possibly could travel.

Perhaps the above observations of at least metre-scale transport of relatively large blocks can explain the enigmatic occurrence of dyke-like outcrops of the large volume Hinckley Range Gabbro (HRG) intrusion. From Figure 2, the outcrops of HRG, as defined by petrology and geochemistry (section 4), are curved and irregular, whereas only the dolerite dykes (even those clearly truncated by mylonites) actually have a planar, dyke-like morphology. Also evident from Figure 2 is the fact that the outcrops of HRG only occur adjacent to mylonites, ultramylonites and/or L-tectonites, possibly implying that their occurrence in the present location is dependant on the steep stretching lineations, rather than igneous activity. The timing of the mylonitic deformation (section 6) disallows the possibility of coeval intrusion and shearing.

4. Mafic petrology and geochemistry

Representative thin sections of two different mafic intrusions types were made for the purpose of identifying the mafic suites to which they belong.

Sample 155743 comes from a large irregular mafic outcrop on the western edge of Shag Hill (Fig. 2). The outcrop trends NW-SE, and is contained within a similarly trending ultramylonite, which, in turn, is bound to the north and south by granitic L-tectonite. The cm-scale felsic veinlets evident in the outcrops are also represented in thin section, with the petrology consisting of dominantly mafic mineralogy, with mm- to cm-scale felsic pods running also present.

The mafic mineralogy consists of coarse to medium grained, sub- to anhedral plagioclase (30%), medium grained olivine (10%), medium grained clino- and orthopyroxene (15% and 7%, respectively), rare quartz (3%), opaques (FeOx; 5%) and a very fine-grained brown altered groundmass (altered feldspar (and biotite?); 30%). The brown material exists only as thin anastomosing bands that surround augen-shaped blobs of the other minerals, and the opaques occur mostly as fracture fill in cracked grains, or within the brown material. The felsic domains consist of medium grained quartz (65%) and feldspar (25%), and fine grained olivine (5%) and pyroxene (5%). The transition from a mafic to a felsic domain is gradual, with the proportions of olivine, plagioclase and pyroxene decreasing, while the proportion of quartz increases.

The outcrop and thin section petrology of sample 155743 is analogous to the gabbroic member of the Hinckley Range intrusion as defined by Glikson et al. (1996). In sample 155743, the sub- to anhedral plagioclase textures, and the occurrence of augen-shaped crystal groupings, surrounded by bands of altered feldspar can be attributed to the high strain imposed by the adjacent shear zones.

Sample 155753 comes from a NE-SW trending dolerite dyke, ~1.5m wide, cutting through the central area of Shag Hill (Fig. 2). The mineralogy consists of plagioclase

(45%), olivine (15%), clinopyroxene (CPX; 15%), orthopyroxene (OPX; 5%), opaques (FeOx; 5%), and groundmass (20%). The groundmass consists of (slightly glassy?) very fine-grained plagioclase, pyroxenes and opaques.

The sample possesses a moderate porphyritic texture, with sub- to euhedral phenocrysts of olivine (~1mm; rare crystals up to 6mm) and plagioclase (~½mm), and mesocrysts of CPX/OPX (<½mm) in amongst the groundmass. The olivine crystals are typically highly fractured (with infill of serpentine and opaques, probably magnetite). Plagioclase is present as euhedral needle-like crystals, and also has a strong ophitic texture, with the subhedral-euhedral mesocrysts of pyroxene in between the euhedral plagioclase phenocrysts.

The petrology of sample 155753 is analogous to the Type C dolerite dykes classified by Glikson et al. (1996), in particular the porphyritic/ophitic texture, the coarse grained (partially serpentinised) olivine, and the coarse grained, needle-like plagioclase crystals.

Twelve different mafic bodies were analysed by a combination of X-Ray Fluorescence Spectrometry, Inductively Coupled Plasma (ICP) Mass Spectrometry and ICP Optical Emission Spectrometry by Ultra Trace Analytical Laboratories (Canning Vale, Western Australia). The geochemical data are presented in Table 1, and Fig. 6a shows that, out of the 12 outcrops sampled, the data fall into three discrete groups, labelled groups 1-3.

Sample 155743 falls within the group 1 samples (Fig. 6a). The outcrops associated with these four samples all possess the same mafic host/felsic dyke petrological relation-

ship, have similar irregular morphologies, are thicker than the dykes of group 2 and 3, and all are situated in conjunction with a shear zone and/or L-tectonite. These observations suggest that all four outcrops are associated with the HRG intrusion. This is supported by the data for a microgabbro from the western Hinckley Range (as reported by Glikson et al., 1996) which correlates with the group 1 samples (Fig. 6b). Of particular note is sample 155725, the small, lineation-rimmed, outcrop contained within the ultramylonite adjacent to the equivalent, but much larger outcrop (sample 155724), as described in section 3.2. The essentially equal geochemistry of the two samples further supports the idea that they are the same body that has been juxtaposed by movement associated with the mylonitisation. In fact, all of the outcrops identified as group 1 (HRG) are located in conjunction with shear zones (Fig. 2). This further supports the theory that the occurrences of HRG are the result of extreme stretching, parallel to the mylonitic mineral lineation, during the mylonitisation, rather than igneous intrusion.

The elevated Cr and Ni values for 155753 (Table 1) are consistent with the levels reported by Glikson et al. (1996), supporting the correlation of this sample to the type C dyke suite. Sample 155753 falls within group 2, suggesting that the other three samples in group 2 are also of the type C suite. This is supported by the fact that all four dykes have the same morphology, trend NE-SW, and have elevated Cr and Ni levels (Table 1; Fig. 6b). On the type C dyke suite, Glikson et al. (1996) reports a marked heterogeneity between samples, and also a geochemical similarity between type C and type A suites, which is reflected in Figures 6a and 6b. A Sm-Nd mineral-whole rock isochron age of c.1000 Ma was obtained from a single type C dyke in the western Hinckley Range (Glikson et al., 1996).

Figure 6b suggests that the group 3 dykes are equivalent to the type B suite of dykes reported by Glikson et al. (1996). Group 3 dykes are all NW-SE trending, which is consistent with the description of the type B suite. Samples 155741 and 155742 do not possess the planar morphology of 155720 and 155752 (as is described by Glikson et al. (1996)), but the location of these two particular outcrops adjacent to two intersecting mylonites can account for the apparent deformation. It should be noted that no thin sections have been made from any group 3 samples, and that such a petrological investigation should be made to strengthen the linkage between group 3 dykes and type B suite. A $^{207}\text{Pb}/^{206}\text{Pb}$ baddeleyite age of 824 ± 4 Ma has been produced for dykes of the type B suite (Glikson et al., 1996), which is equivalent to the Amata dyke swarm described by the same author.

The identification of groups 2 and 3 as the equivalents of type C and B dyke suites, respectively, limits the mylonitic/ultramylonitic deformation to a post- D_3 timing, but does not discriminate between D_{4-7} . Sample 155753 also cuts across the E-W trending felsic dyke (and its associated high strain foliation), thereby restricting the age of intrusion and deformation of the felsic dyke to being >1000 Ma.

The association of particular dyke suites to a particular trend allows a tentative classification of the ENE-WSW trending dyke at the southern margin of Shag Hill, and the NW-SE trending dyke in the NE corner of the hill as type C and type B, respectively, even though they have not been sampled, or observed thoroughly in outcrop.

5. Geochronology

5.1. Analytical procedure

All crushing and mineral separation was undertaken at the Mawson Laboratories at the University of Adelaide, South Australia. Fist-sized representative portions were cut from larger samples and crushed in a tungsten carbide ring mill. The resultant crushing was sieved simultaneously through 75 and 300 μm mesh. The 75-300 μm fraction was reduced in size through hand panning, and the zircon extraction was accomplished through Frantz magnetic and heavy liquid separation. Approximately 70-100 zircons from each sample were hand picked and, along with several grains of the standards Tadmora and CZ3, were positioned in a 25mm diameter araldite-epoxy mount.

The mount was polished to the approximate half-width of the zircon grains. Internal zircon morphology was analysed using a cathodoluminescence (CL) detector on a Philips XL20 scanning electron microscope (SEM) operating at 12.0 kV, located at Adelaide Microscopy, University of Adelaide.

The operating guidelines regarding the SHRIMP are detailed in various publications (e.g., Compston, 2000; Compston et al., 1992; Williams, 1998). The SHRIMP analysis of each spot was repeated 6 times and the results were averaged.

5.2. Sample descriptions

Internal zircon morphologies were studied using the CL detector in a SEM, and several examples (including analysis locations) are displayed in Fig. 7. The degree of luminescence displayed by the zircon crystals is affected by the concentration of certain trace elements (e.g. U, Hf, Y) within the zircon structure (Koschek, 1993). The images were inverted to provide a greater contrast within the crystals, and consequently, the higher concentrations of U were found to be related to the more intense luminescence ('high-CL'), while the opposite was true for lower U concentrations (corresponding to 'low-CL').

5.2.1. 155710: felsic dyke

This sample possesses a high strain fabric at an angle to the widespread foliation, is truncated to the north by a E-W trending ultramylonite, and is truncated to the south by a NE-SW trending mylonite.

Zircons from this sample range between 50-200µm long, are sub- to euhedral, and all are much longer than they are wide. The CL images generally show a subtle zoning in some of the crystals, and in a few cases, rims with no CL pattern surround subtly zoned cores. Exceptions to this generalization include spot 5.1/5.2 (Fig. 7b), and spot 1.1, which shows a 'simple twin' style distribution of high- and low-CL.

5.2.2. 155712 & 155750: mylonitic shear zones

Sample 155712 is from the NE-SW trending mylonite that truncates the felsic dyke (155710, above), which is truncated to the north by the same E-W trending ultramylonite that truncates sample 155710. Sample 155750 is from the same shear zone, but sampled approximately 100m to the west, where the shear zone has swung around to a E-W orientation.

Zircons from both samples range between 50-100 μ m long, and generally are sub-rounded prismatic grains (Fig. 7c and 7d). Core/rim relationships are of a similar style to, but are far more prevalent than in sample 155710. In most cases, the core structure (indicated by oscillatory CL-morphology) appears euhedral, whereas the more featureless rims appear to be the cause of the rounded crystal morphology.

A moderate proportion of the crystals appear to be fractured portions of much larger grains, but the fractured portions are still large enough to allow for accurate and undisturbed analyses. Whether the fracturing can be attributed to the mylonitic deformation is unknown.

5.3. Results

Data for the three samples is given in tables 2-4, with the error presented there given at the 1σ level, while the errors given for grouped data is at the 95% confidence level. All analyses discussed in the following text have been corrected for ^{204}Pb ('common lead'), however the effect of common lead in these analyses is relatively minor. The proportions of ^{206}Pb attributed to common lead (from the ^{204}Pb correction) within the CZ3 standards

averaged at 0.08%, with similar levels found in the unknown populations (which, on average, ranged from 0.01% to 0.5%), indicating that most of the common lead came from the mount surface. As such, the common lead isotope ratios were modeled as the Broken Hill lead composition. The effect of common lead on the mount surface was minimised by rastering the area around the analysis location for 180 seconds before each analysis.

5.3.1. 155710: felsic dyke

12 analyses of 9 zircons from this sample were made, with the spots focused both on the homogenous CL crystals and the crystals with apparent CL rims. All but three analyses were essentially concordant (table 2). The significantly discordant point (710-1.1), along with its substantial error, is attributed to the fact that that particular analysis was the first of the session, and the operating conditions were still being optimised.

With the exception of analysis 710-1.1, the data all fall within a single population (Fig. 8), with a weighted $^{207}\text{Pb}/^{206}\text{Pb}$ age of 1166 ± 13 Ma (MSWD = 2.5), and a weighted $^{206}\text{Pb}/^{238}\text{U}$ age of 1150 ± 25 Ma (MSWD = 11.7). Analysis 710.1.1 had a $^{207}\text{Pb}/^{206}\text{Pb}$ age of 1412 ± 446 Ma.

The analysis of what appeared to be rims around subtly zoned cores yielded no extreme differences between the two. In particular, of three core/rim pairs obtained from the same grains (710-2.1/2.2 and 710-3.1/3.2 and 710-5.1/5.2) two show almost exactly the same age (e.g. 710-3.1/3.2; Fig. 7a). In the case of analyses 710-5.1/5.2, the core is considerably older than the rim (core: 1237 ± 27 ; rim: 1176 ± 13). That particular crystal is of a considerably different size and morphology to the rest of the population (Fig. 7b), and the

interpretation is of a xenocrystic core rimmed by zircon associated with the dyke intrusion.

In addition to 710-5.1, the expulsion of the two other discordant points (710-6.1 & 710-7.1) produces a weighted $^{207}\text{Pb}/^{206}\text{Pb}$ age of 1162.5 ± 7.7 Ma (MSWD = 0.88), and a weighted $^{206}\text{Pb}/^{238}\text{U}$ age of 1144 ± 12 Ma (MSWD = 2.1). It should be noted, however, that the crystal quality or CL morphology show no justification for the exclusion of points 710-6.1 and 710-7.1.

5.3.2. 155712: NE-SW mylonitic shear zone

Ten analyses were made from eight different zircons from this sample, with all being either concordant or only slightly negatively discordant (Fig. 9). The individual analyses have $^{207}\text{Pb}/^{206}\text{Pb}$ ages ranging from c.1140 to c.1330 Ma (table 3), which fall into two age groups (Fig. 9), correlating with the core/rim relationships revealed in the CL images. This is exemplified by analyses 712-5.1/5.2 (Fig. 7d), of which 712-5.1 (rim) and 712-5.2 (core) have $^{207}\text{Pb}/^{206}\text{Pb}$ ages of 1199 ± 10 and 1286 ± 19 Ma, respectively.

The weighted $^{207}\text{Pb}/^{206}\text{Pb}$ age of all group 1 analyses is 1292 ± 45 Ma (MSWD = 3.7). Scrutiny of the CL images identifies one data point to be careful of (712-6.1), as this analysis was performed on a piece of zircon approx 30 μm wide, which appears to be a small fragment of a larger grain. This analysis is only just outside the group 1 average, and its omission does not greatly affect the data – the MSWD is reduced but the error is increased. With the omission of 712-6.1, the weighted $^{207}\text{Pb}/^{206}\text{Pb}$ age becomes 1303 ± 54 Ma (MSWD = 3.1), and the weighted $^{206}\text{Pb}/^{238}\text{U}$ age becomes 1323 ± 34 Ma (MSWD = 3.2).

The group 2 analyses produce a weighted $^{207}\text{Pb}/^{206}\text{Pb}$ age of 1198 ± 24 Ma (MSWD = 1.7), and a weighted $^{206}\text{Pb}/^{238}\text{U}$ age of 1213 ± 60 Ma (MSWD = 16). Examination of the CL images identifies no analyses on dubious crystals, and there are no statistical problems with the analyses that have come from the fractured portions of larger crystals (i.e. spots 712-2.1 and 712-7.1). The only analysis to note is 712-1.1 (Fig. 7c), which appears to be located within what appears to be a core, however, its age plots it in group 2. It is likely that the core has been reset during metamorphism.

5.3.3. 155750: E-W mylonitic shear zone

Thirteen analyses were made from ten different zircons, with all but two analyses being either concordant or near concordant. The individual analyses have $^{207}\text{Pb}/^{206}\text{Pb}$ ages ranging from c.1133 to c.1342 Ma, of which all, barring analyses 2.1 and 2.2, fall into two age groups (Fig. 10), which, again, correlate with the core/rim relationships revealed in the CL images. The core/rim relationship is exemplified by analyses 750-5.1/5.2 (Fig. 7f), of which 750-5.1 (core) and 750-5.2 (rim) have $^{207}\text{Pb}/^{206}\text{Pb}$ ages of 1342 ± 24 and 1198 ± 28 Ma, respectively.

Splitting the data set up into groups based on cores and rims (group 1 and 2, respectively; table 4) produces weighted $^{207}\text{Pb}/^{206}\text{Pb}$ ages of 1304 ± 17 Ma (MSWD = 1.5) for the cores and 1194 ± 17 Ma (MSWD = 1.8) for the rims.

The omission of analyses 2.1 (core) and 2.2 (rim) is justified with the acknowledgment that the crystal was too small, and there was a likely core/rim overlap with both analyses (and probably overlap of analysis 750-2.2 with the epoxy mount; Fig. 7e). The

ages, therefore, are probably both mixed ages, which fits with the observation that the two analyses fall in between the two groupings in Fig. 10.

The exclusion of analyses 2.1 and 2.2 produces a weighted $^{207}\text{Pb}/^{206}\text{Pb}$ age of 1305 ± 11 Ma (MSWD = 1.04), and a weighted $^{206}\text{Pb}/^{238}\text{U}$ age of 1286 ± 86 Ma (MSWD = 30) for the cores, while for the rims the weighted $^{207}\text{Pb}/^{206}\text{Pb}$ age comes at 1191 ± 10 Ma (MSWD = 1.02), and the weighted $^{206}\text{Pb}/^{238}\text{U}$ age of 1183 ± 68 Ma (MSWD = 42).

It should be noted that analysis 1.2 has been included in the rim grouping, despite the fact that the spot appeared to be located within an apparent zircon core. The weighted $^{207}\text{Pb}/^{206}\text{Pb}$ ages for spots 1.1 (rim) and 1.2 (core) are 1133 ± 44 and 1176 ± 17 Ma, respectively. The zircon morphology is no different to the other analysed crystals, and the crystal is $\sim 200\mu\text{m}$ long, indicating that it is unlikely to be solely a product of the rim-forming event. Again, the interpretation is of resetting of the core during metamorphism.

5.4. Standard errors

The aforementioned ages do not take in account the errors associated with the Tamora standard. This error (2σ ; 0.79%) was added to the unknowns, through root mean square computations, to give final (weighted $^{207}\text{Pb}/^{206}\text{Pb}$) ages of:

Sample	Group 1	Group 2
155710	1162 ± 12 Ma	-
155712	1303 ± 55 Ma	1198 ± 26 Ma
155750	1305 ± 15 Ma	1191 ± 14 Ma

5.5. Discussion

The eight analyses of sample 155710 are interpreted as the crystallisation age of the zircons, which is analogous to the emplacement age for the felsic dyke. The field relationships show that the dyke intrusion post-dates the foliation. As such, no record of the widespread foliation is to be expected in those zircons. The absence of any rims corresponding to later zircon growth implies that the zircons also show no evidence of the high strain fabric contained within the dyke. The age of the high strain fabric within the dyke is restricted to being between c.1162 Ma and the age the crosscutting type C mafic dyke (c.1000 Ma).

The similar zircon morphology and identical ages of zircons in samples 155712 and 155750, coupled with the fact that they were sampled from the same shear zone, allows the following discussion to represent both samples.

Two different age populations are present in both of the samples, which correlate with the core/rim relationships shown in the CL images. The ages given by these core/rim relationships lead to the interpretation of either: (1) the intrusion of Pitjantjatjara Suite granite (1190-1120 Ma, Bodorkos et al., 2006; Edgoose et al., 2004) with a degree of partial melting of Wankanki granite, (i.e. producing xenocrystic Wankanki cores with Pitjantjatjara-aged rims); or, (2) the intrusion of Wankanki granite providing the c.1300 Ma cores, and metamorphism associated with the Musgravian Orogeny producing the c.1190 Ma rims.

The apparent analysis of both a core and a rim with c.1160 Ma ages supports the former (i.e. 750-1.1/1.2), however, both the abundance of Pitjantjatjara Suite granite, and the

ratio of c.1190 Ma to c.1300 Ma cores, are far too low to sustain the idea. The elongate, sub- to euhedral shape of the zircon cores, and the subtle oscillatory zonation, implies that the group 1 ages represent the igneous crystallisation age of the zircons (which is taken to be equivalent to the emplacement age of the granite). The anhedral, non-zoned, rims that surround the cores (group 2) are consistent with metamorphic growth.

Thus, the CL core/rim morphology, in addition to the fact that the foliated granite is petrologically far similar to the GSWA-dated Wankanki suite than to the porphyritic Pitjantjatjara suite, indicates that the data represent c.1195 Ma metamorphic zircon growth over c. 1304 Ma igneous zircons.

6. Timing of deformation

The main constraint upon the mylonitisation at Shag Hill are the mafic dykes that are cut and deformed by the shear zones. The identification of the type B dyke suites that are deformed by the mylonites and ultramylonites limits the shear zone genesis to <c.824 Ma (post-D₃), but does not permit discrimination between D₄-D₇.

This relative timing, which is consistent with the crystallisation age of sample 155710, implies that the mylonitic/ultramylonitic deformation at Shag Hill cannot be considered Musgravian deformation. This indicates that there is no record of the mylonitic deformation within the zircons of samples 155712 and 155750 (apart, perhaps from the fracturing of crystals), and that the metamorphic overgrowths present in these samples can therefore be attributed to the terrain scale foliation, thus linking the foliation to the widespread c.1200 Ma orogenic activity (Musgravian Orogeny, Betts et al., 2002; White et al., 1999).

Clarke et al. (1995) suggests the possibility that the D₄-D₇ events may represent a continuous, evolving orogenic system. The characteristics of the Shag Hill shear zones are consistent with a number of the features described from D₄-D₆, including the E-W trending amphibolite facies D₄ ultramylonites, but in particular the E-W trending mylonites of the Petermann Orogeny (Clarke et al., 1995; Edgoose et al., 2004; Glikson et al., 1995; Scrimgeour et al., 1999). The latter are characterised by northward directed thrusting and extensive pseudotachylite veining, both of which are features observed at Shag Hill. P-T estimates associated with Shag Hill during the Petermann Orogeny are uncertain, with the reported estimates (at least 6kbar, 650°C, Scrimgeour and Close, 1999) coming from north of the Mann-Hinckley Fault, which is considered to be a deeper crustal block at that time (Camacho and Fanning, 1995).

Field relationships indicate that the mylonites of Shag Hill predate the ultramylonite (Fig. 2), but an absolute timing of the two has not been delineated by this study. The similar kinematics and transport directions suggest the two may have been a part of the same evolving deformation. The more plastic deformation in the mylonites, compared to the ultramylonite, indicates that the former operated under higher grade conditions than the latter. It is therefore possible that the transition from mylonite to ultramylonite reflects evolution during the Petermann Orogeny, with the ultramylonite forming as the orogen was exhumed.

7. Microanalysis

7.1. Optical microstructural analysis

The strain across Shag Hill is manifested as three different structural features within the Wankanki Supersuite granite. Microstructural observations for the three features, ultramylonite, mylonite and L-tectonite, are presented below. The convention used is such that the terms dextral and sinistral refer to the kinematics within the thin section, and south side up and north side up refers to kinematics observed in outcrop. Dextral kinematics in thin section are equivalent to south side up in outcrop.

7.1.1. *Foliated granite; sample 155747*

This foliated granite is representative of the Wankanki granite of Shag Hill, which hosts the various mylonites, ultramylonites and L-tectonites. The foliation in the sample is weak, and is defined by the slight elongation of large quartz crystals (4-6mm). Some quartz blasts possess slight subgrain development, most of which are elongate and inclined 30-40° to the weak foliation. In general, quartz grains and subgrains have smooth, low angle boundaries, and rarely, the subgrains have fine, irregular boundaries.

7.1.2. *Ultramylonite; samples 155705, 155706*

Both samples come from within the E-W trending ultramylonite along the northern boundary of Shag Hill, and both share similar mineralogy and microstructures. The ultramylonitic foliation is defined by alternating bands of light coloured and dark olive-

green material, typically <1mm thick. Within these bands, the minerals exist as very fine-grained, highly altered crystals, or as elongate ribbons. The latter form is comprised by quartz only, while the former is comprised of altered feldspar (lighter) and altered amphibole (olive brown) (Fig. 11b). The amphibole in the sample is assumed to be due to the proximity of a (concealed) mafic body. The mafic material has been transported into the shear zone in a manner analogous to the displacement of the Hinckley Range Gabbro, but for which the ultramylonitic deformation has left no recognizable form.

Both samples have a bimodal distribution of porphyroblasts, with occasional large blasts (5-8mm) of feldspar, and frequent smaller blasts (1-3mm) of feldspar and amphibole. All asymmetrical porphyroblasts, in addition to asymmetric folds and inclined foliations (defined by elongate subgrains within quartz ribbons inclined 45° to the foliation), show a dextral sense of shear.

Numerous microfaults cut across sample 155705, perpendicular to, and completely unaffected by the foliation, displacing both the foliation and the rotated porphyroblasts. Both the foliation and the microfaults are cut by multiple high-angle, straight edged epidote filled fractures, which clearly postdate the mylonitic foliation, in rare instances even managing to fracture and offset isolated porphyroblasts (Fig. 11b). Neither of these two features are observed in sample 155706.

7.1.3. Mylonite; samples 155750, 155712

These mylonites have mineralogies equivalent to the foliated granite through which they cut. The quartz exists only as elongate ribbons, the feldspar as singular crystals, and the biotite as very thin bands (<1/10mm thick) that run parallel to the foliation (Fig. 11a).

The quartz ribbons (1-2mm thick) possess either smooth, low angle boundaries (in which case the ribbon may or may not possess subgrains), or irregular, undulose boundaries (in which case the ribbon always possesses subgrains with irregular boundaries).

The feldspar crystals have a trimodal distribution (Fig. 11d): (1) large, strain free porphyroblasts (7-10mm) of plagioclase, K-spar and minor microcline; (2) elongate lensoid packages aligned with the foliation, which are comprised of diamond-shaped crystals (2-6mm) formed by a repeating conjugate fracture set; or (3) very fine-grained fractured/altered feldspar that fills in the conjugate fractures.

Sample 155712 possesses the same features as 155750, however, on the micro scale, the mylonitic character is largely confined to relatively narrow bands that anastomose around augen-shaped packages of far less deformed crystals. As such, rotated porphyroblasts, though present (Fig. 11e), are not common, and the kinematics are defined most commonly by asymmetric folds and oblique foliations, which identify a dextral sense of movement (Fig. 11c).

7.1.4. L-tectonite; sample 155751

The sample has the same granitic mineralogy as the foliated granite in which it is situated. The mineral morphology is similar to sample 155750, however: (1) quartz ribbons are generally thicker (4-5mm) and trend straighter and longer across the slide; (2) the predominance of diamond shaped fractures is reduced, the feldspar mostly exists either as moderate sized porphyroblasts (2-4mm) or as fine grained fractured crystals; and (3) biotite bands are thicker ($\frac{1}{2}$ -1mm), less regularly spaced, and trend straighter along the lineation.

Kinematics are poorly developed in this sample (both at the outcrop- and micro-scale), but the rare development of a weak oblique foliation implies a dextral shear sense. Rotated porphyroblasts and asymmetric features are nonexistent in this sample.

7.2. Electron backscatter diffraction analysis

7.2.1. Methodology

For detailed descriptions of the necessary experimental procedures regarding electron backscatter diffraction (EBSD; e.g. sample preparation, experimental setup, indexing, automated EBSD mapping and noise reduction) there are several review papers covering most relevant topics (e.g. Lloyd, 1987; Prior et al., 1999; Schmidt and Olesen, 1989).

Crystallographic orientation data was obtained through electron backscatter pattern (EBSP) analysis on a Phillips XL30 SEM with an accelerating voltage of 20kV, beam current 20nAmps, a working distance of 20mm and a tilt of 70°. EBSD samples were prepared from standard XZ-sectioned optical thin sections by colloidal silica polishing for approximately 45 minutes per sample. The samples were then coated with the thinnest possible coat of carbon, and the specific areas of interest were surrounded by carbon dag. The EBSPs were automatically indexed with the CHANNEL 5 software (Schmidt and Olesen, 1989) of HKL Technology, Burnt Hills, New York, and orientation maps were created by moving the beam with a 4µm step size (8µm step size for 155751), and map sized ranged from 44,000 pixels to 58,000 pixels. The successful indexing of phases (quartz, albite, anorthite, orthoclase and biotite) was dictated by a mean angular deviation (MAD; the difference between observed and theoretical EBSP) cut-off of 1.5.

The average overall map MAD was 0.67, of which quartz averaged at 0.64 and feldspars and biotite averaged at 0.85 and 0.87, respectively. The degree of zero-indexing of the data ranged from 20-40%, most of which can be related to the presence of cracks, or to non-quartz phases (i.e. feldspar indexed at <50%, biotite indexed at <1%). Only minor systematic zero-indexing of quartz occurred, and is assumed to be related to small areas of charge build up on the slide.

The raw orientation data were processed with the noise reduction features of the CHANNEL 5 software to remove erroneous data (mis-indexing) and to fill in certain areas of no data (zero solutions). Mis-indexing was reduced with a wildspike correction, and zero solutions were reduced with 2 or 3 iterations of a 4-5 nearest-neighbour extrapolation. The noise reduction features were used with caution so as not to introduce unwanted artifacts or exaggerations into the data. The noise reduction generally reduced the proportion of zero indexing by two or three times its original value, to levels ranging from 1.5% to 22%. The wildspike correction had the greatest effect in reducing the proportion of biotite (which almost solely was indexed as individual isolated points inside quartz grains).

7.2.2. Analysis

Three automated beam maps were made from three different samples from a single high strain zone (samples 155747, 155750, 155751; Fig. 2), with the different samples each representing a different degree of strain within the zone.

Within the foliated granite (155747), map747 was produced within a single large quartz grain (~3mm). The weak foliation of the sample runs approximately parallel to the

length of the grain, and the moderate subgrain development is elongate at approximately 45° to this foliation.

The resultant Euler angle map (Fig. 12a) shows three different orientation domains, the large purple area to the right (*right domain*), the moderate green area to the left (*left domain*) and the small lighter purple area in the top left (*top-left domain*; partially obscured by non-indexing), which are centered around the single elongate grey crystal in the centre (feldspar; Euler angles not shown). The foliation in the slide runs N-S.

Overlain on the Euler angles of Fig. 12a are the grain and subgrain boundaries. Subgrain boundaries, which enclose areas of <2° misorientation, are shown in red, grain boundaries, which enclose areas of <10° misorientation, are shown in black and Dauphiné twin boundaries are shown in yellow (such convention is used consistently throughout this report). In the right domain, the elongate subgrains can be seen running at an angle to the foliation, and several small elongate grains (outlined by yellow boundaries) can also be seen running parallel to these. The left domain shows more extensive subgrain development, and the subgrains are smaller and rounded. The left domain, like the right domain, also possesses smaller grains within the large grain outlined by yellow boundaries, but these too are rounded rather than elongate. The top left domain, although masked by zero-solutions, appears to show similar Euler orientation as the right domain (defined by similar shading; see Prior et al., 1999), but has a grain/subgrain development similar to the left domain.

Map750 (sample 155750; mylonitic form of 155747) was produced over multiple elongate quartz bands, separated by bands of feldspar and minor biotite (Fig. 13a). The quartz bands are of two varieties; those with relatively smooth edges and moderate sub-

grain development, and those with angular/irregular edges. The elongation of the quartz within the bands runs parallel to the mylonitic foliation of the sample.

The Euler angle map clearly shows the two different styles of quartz banding. The thicker (~200µm) band just above centre shows large elongate grain boundaries running sub-parallel to the length of the ribbon, coupled with extensive small, rounded subgrain boundaries (*ribbon domain*). The other three bands comprise of considerably finer and more rounded grains (<30µm), and possess relatively few subgrain boundaries (*fine grain domain*). While the fine grain domains predominantly consist of small, rounded, subgrain-free grains, they all contain ‘cores’ of larger, elongate grain boundaries (*centre domain*). Although smaller, these cores appear similar to the large elongate grains in the ribbon domain in shape, and in orientation, and also, again similar to the ribbon domain, possess a higher concentration of subgrain boundaries relative to the finer rounded grains.

Sample 155751 comes from the L-tectonite immediately adjacent to the mylonite studied in map750. Map751 was run over multiple elongate quartz bands; no other phases were present in the sample area. The lineation in the sample runs parallel to the horizontal elongate ribbons in Fig. 14a.

The Euler angle map (Fig. 14a) shows three distinct, thick (~500µm) quartz bands, comprised of elongate grains analogous to the ribbon grains of map750 (*ribbon domain*). The subgrains at the centre of the thick ribbons are elongate parallel to the macroscopic foliation, whereas towards the edges, the subgrains become smaller and more rounded. Separating the ribbon bands are small equant grains (<80µm), which are analogous to the fine grains of 750 (*fine grain domain*).

7.2.3. Results

The $\{0001\}$ (c-axis) and $\{1-210\}$ (a-axis) orientations for the three different samples are displayed in Fig. 12 to Fig. 14, in lower hemisphere, equal area projections. The idealised m- and r- faces and a-directions of a quartz crystal is summarised in Fig. 15a. X0 and Z0 of the pole figures refer to the X and Z axes of the finite strain ellipsoid with respect to macroscopic sample foliation, with Y0 coming out of the plane of the page and representing the intermediate axis of the finite strain ellipsoid (Fig. 15b). Thus the horizontal X0 line represents the foliation plane, and the vertical Z0 line is the pole to the foliation plane. Where appropriate, data subsets have been made, and their names refer to the previously defined domains.

155747

The pole figure of the complete map747 data set (Fig. 12b) shows two dominant orientations, which correspond to the left, right and top left domains of Fig. 12a. The tight grouping of the data, with respect to the different domains, is merely due to the fact that there are only 3 different grains being measured, and the misorientation within those grains is relatively small ($<10^\circ$ by definition).

155750

Orientation data for map750 are displayed in Fig. 13b (whole map data set), and Fig. 13c, 13d and 13e (the ribbon, centre domains and fine-grain, respectively). The contoured c-axis pole figures show a strong preferred orientation within all three domains, but more so for the ribbon domain. It is also clear that the ribbon and centre domains are essen-

tially equivalent (as noted from Fig. 13a), and both are distinct from the fine-grain domain, thereby suggesting that the fine-grained bands were originally equivalent to the ribbon bands, but have since been transformed.

The c-axis pattern for the ribbon domain (and thus the central domain; Figs. 13c and 13d) shows a single point maxima coincident with the Y-axis (i.e. parallel to the foliation, perpendicular to the lineation), and the equivalent a-axis patterns show 6 maxima, corresponding to the hexagonal symmetry of quartz.

Studies on naturally and experimentally deformed quartz have shown that particular patterns of c- and a-axis maxima will develop for a particular stress regime and temperature range (Law, 1990; Lister and Hobbs, 1980; Passchier and Trouw, 1998; Twiss and Moores, 1992) – (Fig. 15c and 15d). In the case of non-coaxial deformation, the asymmetric grouping of the c- and a-axis maxima can be used as a kinematic indicator, and hence, the shear sense associated with the deformation can be inferred. The specific pattern shown by the ribbon domain of map750 can be interpreted with equivalent prismatic slip systems in the a-direction (i.e. (m)[a] slip) either by coaxial (thereby involving slip orientated symmetrically about the maximum extension (\hat{s}_1) and maximum shortening (\hat{s}_3) axes) or non-coaxial slip (Passchier and Trouw, 1998; Twiss and Moores, 1992). While the c-axis pattern alone is insufficient to presume coaxial over non-coaxial deformation (or vice versa), the asymmetric positioning of the a-axis maxima suggests non-coaxial deformation, which is consistent with macro- and microstructural observations of the quartz ribbons, which rule out coaxial shear (e.g. asymmetrically folded ribbons, ribbons ramping up and over other ribbons; Fig. 11). In addition, the asymmetric orientation

of the a-axis maxima indicates a dextral shear sense (Fig. 15c), which is also consistent with the macro- and microscopic kinematics of the sample.

The c-axis pattern for the fine-grain domain (Fig. 13e) exhibits a single asymmetric girdle pattern, (Fig. 15c), roughly normal to the foliation plane, but inclined away from the Z-axis, and the a-axis contouring again shows ~6 maxima positioned at the edges of the pole figure. This particular combination of c- and a-axis patterns is also indicative of non-coaxial shear (Passchier and Trouw, 1998; Twiss and Moores, 1992), but in this case, the inclination of the girdle in an anticlockwise direction from the Z-pole implies a sinistral sense of shear.

155751

The orientation data for map751 is displayed in Fig. 14b (whole map data set), and Figs. 14c and 14d (the ribbon and fine grain domains, respectively). The two domains show somewhat similar characteristics, with the data concentrated in two girdles normal to the foliation plane, and the a-axes predominantly concentrated in small circles located around the edges of the X-axis, referred to as a cleft girdle pattern (Passchier and Trouw, 1998; Twiss and Moores, 1992).

The combination of the c- and a-axis patterns in the fine grain domain is indicative of deformation characterised by (coaxial) simple extension, and is termed a cleft girdle pattern (Fig. 15b, Passchier and Trouw, 1998). Under such deformational conditions, the small circles defined by the c- and a axes distribute around \hat{s}_1 , which, in this case, confirms that the extension was parallel to the mineral elongation lineation, within the XY-plane (i.e. the foliation plane).

No definitive conclusions can be made from the data regarding the ribbon domain; owing the large grain sizes, only five or six large grains are present within the map area. In terms of defining a CPO, this therefore means that there essentially are only five or six data points, a fact which is evident in Fig. 14c, as the axes are concentrated in 4 or 5 orientations.

It is likely that the two mineral domains both formed under the same extensional regime, and subsequently, if orientation data for a much larger number of ribbon grains can be obtained, the c- and a-axis distributions of the ribbon domain would mimic that of the fine grain domain. When the current ribbon grain orientation data is superimposed onto the data for the fine grain domain, the orientations of all the points all lie within the range of the cleft girdle pattern defined by the data for the fine grain domain.

7.3. Discussion

The rheological difference between quartz and feldspar is evident across the different grades of strain. Quartz typically forms long ribbons, whereas the feldspars do not stretch and are far more likely to form round porphyroblasts (Fig. 11a). Where the feldspar is forced to stretch, the crystals fracture rather than lengthen (i.e. the diamond shaped crystals of 155750 and 155751; Fig. 11d). The following discussion is based upon the observations made both under the optical microscope and from the EBSD analysis.

7.3.1. Foliated granite

As previously stated, the EBSD data from only three different grains in map747 do not permit conclusions to be made regarding the terrain-scale foliation. What can be drawn from this analysis, however, are some basic observations regarding the strain within the sample.

Both the left and right domains possess extensive subgrain formation, however the subgrains in the right domain are elongate and inclined to the foliation, whereas the left domain possess subgrains that are smaller and far more rounded. This same feature is observed optically. The elongation of these subgrains is probably indicative of a greater amount of strain in the right domain, and indicates a degree of strain partitioning on the micro-scale.

The Dauphiné twins, which define the small grains present within the larger grains, are characterised by an apparent 60° rotation (actually a 180° rotation) around the c-axis. The generation of the Dauphiné twins, which cannot be observed optically without acid etching (Neumann, 2000), is regarded as a low-grade feature of quartz crystals, and is attributed to applied pressure of quartz crystals at low temperature. It is not known whether deformation resets the crystal distortion caused by Dauphiné twinning, however studies have documented the decrease in the occurrence of the twins with an increase in strain (e.g., Heidelberg et al., 2000; Neumann, 2000). This is consistent with the EBSD observations, which show far fewer occurrences of the Dauphiné twins in samples 155750 and 155751, compared with 155747 (compare Figs. 13a and 14a, with Fig. 12a).

The small grains defined by the Dauphiné twin boundaries have morphologies identical to the subgrains within the two domains – i.e. elongate in the right grain, and rounded

and irregular in the left grain. This probably reflects the fact that the elongation occurred after the formation of the subgrains and Dauphiné twins.

7.3.2. Ultramylonite

The relationship between the ultramylonitic fabric and the epidote in sample 155705 is consistent with the interpretation of progressive deformation during the exhumation of the shear zones (section 6). The epidote clearly postdates the ultramylonitic foliation (Fig. 11b), implying that the lower grade conditions (inferred from the presence of epidote) were present after the deformation that produced the ultramylonite. The absolute time difference between the two events cannot be determined, however, the fact the epidote cuts and displaces the microfaults (which, in turn, cut and displace the ultramylonitic fabric) indicates another low temperature deformation ‘event’ operated between the two. Therefore, at the very least, we can assume that the epidote generation did not immediately post-date the ultramylonitic deformation.

7.3.3. Mylonite

Microscopic observations of sample 155750 and the orientation images (Fig. 13a) both imply that the fine grained domain (of map750) represents a later stage of crystal growth, which has overprinted the crystals of the ribbon domain. This is substantiated by the observation that the ribbon-like ‘cores’ within the fine-grained domains are essentially equivalent to the ribbons in size, shape (Fig. 13a) and orientation (Figs. 13c and 13d). Whether the fine grain domain represents evolving conditions in a single deformational event, or reworking of the shear zone at a later date cannot be deduced from these

data alone. If it does represent reactivation at a later stage, it must imply an extra, separate, deformational event, as the original deformation in that shear zone is dextral, and the deformation in the E-W trending ultramylonite (which cuts the studied mylonite) is dextral.

In the case of non-coaxial deformation, a transition from crossed girdle to single point maxima c-axis patterns corresponds to higher temperature and lower strain rate deformation (Fig. 15c, Passchier and Trouw, 1998; Twiss and Moores, 1992). The deformation relating to the fine grain domain can subsequently be constrained to low temperature conditions ($<300^{\circ}\text{C}$), while the point maxima close to the Y-axis restricts the deformation associated with the ribbon grains to medium to high-grade conditions ($300\text{--}650^{\circ}\text{C}$).

The fine grain domain, therefore, represents a later deformation, which operated at a lower temperature than, and with a shear sense opposite to, the earlier recorded phase, and for which there are no outcrop- or thin section-scale kinematic indicators to support the opposite shear sense. The lack of sinistral-style microstructures does not, however, exclude the possibility of sinistral deformation; it may be that the only record the deformation left of itself is in a crystallographic form, but also, any evident microstructures or shape preferred orientations will be hard to observe, as the sinistral kinematics are only present in the fine grain domain (grains $<30\mu\text{m}$).

It is important to note that the second stage of deformation is overprinting grains that already have a strong CPO (i.e. the ribbons), and that there is the possibility of a preferred orientation inheritance within the fine grain CPO data. Fig. 13e shows a strong clustering of data adjacent to the Y-axis (compare to Fig. 13c), which does add some doubt to the kinematic significance of the fine grain domain. However if this clustering is

reduced in intensity, or removed, the CPO pattern would still suggest a sinistral shear sense. Regardless of whether CPO inheritance has occurred or not, the overall interpretation of a sinistral regime is probably still valid.

Optical microstructural observations for map750 reveal: (1) an almost identical morphology between the subgrains within the ribbon-like cores (which are readily identifiable as the whole grain moves into extinction at once) and the fine grains surrounding them (which all have different extinction positions); and (2) that the boundaries between the fine grains are smooth and regular (suggesting the lack of grain boundary migration processes, i.e. annealing) and irregular, bulging boundaries between the ribbon grains (suggesting that they have annealed prior to the late stage of deformation. The first point suggests that the fine grains may be the result of subgrain rotation at the boundaries of what were originally quartz ribbons. This may be due to shear stresses at the interface between the quartz and feldspar bands, as a result of the rheological differences between the different minerals. The second observation supports the suggestion that the later deformation operated at a lower temperature (thereby disallowing the chance for the fine grains to anneal). This, again, is consistent with the inference of later stage mylonitic deformation as exhumation of the shear zone progresses.

7.3.4. L-tectonite

The acknowledgement that the L-tectonite was produced under simple (coaxial) extension is consistent with the proposed shear zone model, (section 3.2), that suggests strain partitioning between coaxial and non-coaxial deformation within a shear zone lead to the relative positioning of the L-tectonites and mylonites, respectfully. This is consistent with

the microstructural observations, which show that the ribboning of quartz is far more pronounced, and also reveals no features associated non-coaxial or compressional deformation (e.g. asymmetric folds or porphyroblasts).

This model implies that, rather than discrete, thin shear zones running parallel to each other, the strain was accumulated (although partitioned) in much larger, wider zones, with the different types of deformation isolated in different areas of the shear zones.

A bimodal distribution is seen between the equant $<80\mu\text{m}$ crystals and the 200-300 μm ribbon-like crystals (Fig. 14a). This, again, is consistent with later deformation at lower temperatures, which produced small, high-dislocation density, grains around the ribbons, which were not subsequently annealed, as the temperature was too low. Both the large and small grains show similar CPOs, implying formation in a similar strain field. It is unclear whether these formed in an evolving down-temperature (exhuming?) deformation path, or in two distinct deformational events.

8. Conclusions

Different generations of shear zones and different suites of mafic bodies are identified throughout the mineralogically homogeneous Wankanki Supersuite granite of Shag Hill. While strain within individual shear zones is heterogeneous, both in outcrop and thin section, all shear zones possess almost exclusively south side up (dextral) kinematics. The interpretation of quartz C-axis orientations indicates the possibility of a separate crystallographic fabric with sinistral-style kinematics.

U-Pb zircon geochronology identified crystallisation ages of c.1304 Ma for the Wankanki Supersuite granite, and also a record of Musgravian-aged orogenic metamor-

phism at c.1195 Ma, which is interpreted as being representative of the widespread foliation of the area. The geochronology failed to determine the absolute timing of the mylonitic deformation in the shear zones, and also a separate high strain fabric within a felsic dyke truncated by the mylonitic deformation.

The shear zones are interpreted to be associated with the Neoproterozoic Petermann Orogeny, based on the correlation of their features with the documented features of that event. This is supported by the maximum age for the mylonitic deformation of c.824 Ma, determined by the identification of Type B suite mafic dykes with intrusion ages delineated by previous studies.

Microstructural and mineralogical evidence both indicate at least two stages of deformation within both the mylonitic and ultramylonitic shear zones. The later of the deformations operated at lower temperature and/or lower grade conditions than the earlier, which is interpreted to represent exhumation of the shear zones (perhaps as a result of movement of the Woodroffe Thrust) during the Petermann Orogeny

Optical and electron backscatter diffraction analysis, has delineated heterogeneities within the mylonitic shear zones, with partitioning of coaxial and non-coaxial deformation within larger high strain zones resulting in the adjacent positioning of L-tectonic and mylonitic zones.

Acknowledgements

I would like to thank my supervisors, Alan Collins and Dave Kelsey, for all their help throughout the year. Many thanks to Hugh Smithies, Heather Howard and Simon Bodorkos, of the Geological Survey of Western Australia, for all the monetary, logistical

and intellectual support provided for this project. Peter Self, of Adelaide Microscopy, and Steve Reddy, of Curtin University, for their assistance in setting up, running, and interpreting the EBSD analyses. The honours bursary provided by the GSA Specialist Group in Tectonics and Structural Geology was of valuable assistance. Thanks to Althea for all putting up with me in the field, and for allowing me to indulge in the asinine activities one partakes in when alone in an isolated area of the country.

References

- Ballhaus, C.G. and Glikson, A.Y., 1995. The petrology of layered mafic-ultramafic intrusions of the Giles Complex, western Musgrave Block, Western Australia. *AGSO Journal of Australian Geology and Geophysics*, 16, 69-89.
- Betts, P.G., Giles, D., Lister, G.S. and Frick, L.R., 2002. Evolution of the Australian lithosphere. *Australian Journal of Earth Sciences*, 49, 661–695.
- Bodorkos, S., Love, G.J. and Wingate, M.T.D., 2006. 180300: porphyritic metamonzonite, Mount Gosse Geochronology dataset 653, Compilation of geochronology data, June 2006 update. Western Australia Geological Survey.
- Camacho, A., Compston, W., McCulloch, M. and McDougall, I., 1997. Timing and exhumation of eclogite facies shear zones, Musgrave Block, central Australia. *Journal of Metamorphic Geology*, 15, 735-751.
- Camacho, A. and Fanning, C.M., 1995. Some isotopic constraints on the evolution of the granulite and upper amphibolite facies terranes in the Eastern Musgrave Block, central Australia. *Precambrian Research*, 71, 155-181.

- Clark, D.J., Hensen, B.J. and Kinny, P.D., 2000. Geochronological constraints for a two-stage history of the Albany–Fraser Orogen, Western Australia. *Precambrian Research*, 102, 155-183.
- Clarke, G.L., 1992. Field relationships and the tectonic history of the Hinckley Gabbro, felsic to mafic granulites and granitoids, west Hinckley Range and Champ de Mars areas, Tomkinson Ranges, Musgrave Block, WA. *Bureau of Mineral Resources Australia Record*, 1992/33.
- Clarke, G.L., Buick, I.S., Glikson, A.Y. and Stewart, A.J., 1995. Structural and pressure-temperature evolution of the host rocks of the Giles Complex, western Musgrave Block, central Australia: evidence for multiple high-pressure events. *AGSO Journal of Australian Geology and Geophysics*, 16, 127-146.
- Collerson, K.D., Oliver, R.L. and Rutland, R.W.R., 1972. An example of structural and metamorphic relationships in the Musgrave Orogenic Belt, central Australia. *Journal of the Geological Society of Australia*, 18, 379-393.
- Compston, W., 2000. Interpretations of SHRIMP and isotope dilution zircon ages for the geological time-scale: 1. The early Ordovician and late Cambrian. *Mineralogical Magazine*, 64, 43-57.
- Compston, W., Williams, I.S., Kirschvink, J.L., Zichao, Z. and Guogan, M.A., 1992. Zircon U-Pb ages for the Early Cambrian time-scale. *Journal of the Geological Society of London*, 149, 171-184.
- Edgoose, C.J., Scrimgeour, I. and Close, D., 2004. *Geology of the Musgrave Block, Northern Territory*. Northern Territory Geological Survey Report, 15.

- Forman, D.J., 1965. Ayres Rock, N.T. 1:250,000 Geological Series. Bureau of Mineral Resources Australia Explanatory Notes, SG52-8.
- Forman, D.J., 1972. Petermann Ranges 1:250,000 Geological Series. Bureau of Mineral Resources Australia Explanatory Notes, SG52-7.
- Giles, D., Betts, P.G. and Lister, G.S., 2004. 1.8–1.5-Ga links between the North and South Australian Cratons and the Early–Middle Proterozoic configuration of Australia. *Tectonophysics*, 380, 27-41.
- Glikson, A.Y. et al., 1995. Geological framework and crustal evolution of the Giles mafic-ultramafic complex and environs, western Musgrave Block, central Australia. *AGSO Journal of Australian Geology and Geophysics*, 16, 41-67.
- Glikson, A.Y. et al., 1996. The Geology of the western Musgrave Block, central Australia, with particular reference to the mafic-ultramafic Giles Complex. *Australian Geological Survey Organisation Bulletin*, 239. Australian Government Publishing Service, Canberra, 206 pp.
- Gray, C.M., 1977. The geochemistry of central Australian granulites in relation to the chemical and isotopic effects of granulite facies metamorphism. *Contributions to Mineralogy and Petrology*, 65, 79-89.
- Gray, C.M., 1978. Geochronology of granulite-facies gneisses in the western Musgrave Block, Central Australia. *Journal of the Geological Society of Australia*, 25(403-414).
- Heidelbach, F., Kunze, K. and Wenk, H.-R., 2000. Texture analysis of a recrystallized quartzite using electron diffraction in the scanning electron microscope. *Journal of Structural Geology*, 22, 91-104.

- Howard, H., Smithies, H., Pirajno, F. and Skwarnecki, S., 2006. Bell Rock, W.A. Sheet 4645. Western Australia Geological Survey.
- Koschek, G., 1993. Origin and significance of the SEM cathodoluminescence from zircon. *Journal of Microscopy*, 171, 223-232.
- Law, R.D., 1990. Crystallographic fabrics: a selective review of their applications to research in structural geology. In: R.J. Knipe and E.H. Rutter (Editors), *Deformation Mechanisms, Rheology and Tectonics*. Geological Society of London Special Publication, London, pp. 335-352.
- Lister, G.S. and Hobbs, B.E., 1980. The simulation of fabric development during plastic deformation and its applications to quartzite: the influence of deformational history. *Journal of Structural Geology*, 2(3), 355-370.
- Lloyd, G.E., 1987. Atomic number and crystallographic contrast images with the SEM: A review of backscattered techniques. *Mineralogical Magazine*, 51, 3-19.
- Maboko, M.A.H., Williams, I.S. and Compston, W., 1991. Zircon U-Pb chronometry of the pressure and temperature history of granulites in the Musgrave Ranges, central Australia. *Journal of Geology*, 99(5), 675-697.
- Major, R.B. and Connor, C.H.H., 1993. The Musgrave Block. *The Geology of South Australia, Volume 1. The Precambrian*, Bulletin 54. The Geological Survey of South Australia, 156-167 pp.
- Myers, J.S., Shaw, R.D. and Tyler, I.M., 1996. Tectonic evolution of Proterozoic Australia. *Tectonics*, 15, 1431-1446.

- Neumann, B., 2000. Texture development of recrystallised quartz polycrystals unravelled by orientation and misorientation characteristics. *Journal of Structural Geology*, 22, 16956-1711.
- Passchier, C.W. and Trouw, R.A.J., 1998. *Microtectonics*. Springer, Berlin, 289 pp.
- Prior, D.J. et al., 1999. The application of electron backscatter diffraction and orientation contrast imaging in the SEM to textural problems in rocks. *American Mineralogist*, 84, 1741-1759.
- Schmidt, N.H. and Olesen, N.O., 1989. Computer-aided determination of crystal lattice orientation from electron channeling patterns in the SEM. *Canadian Mineralogist*, 27, 15-22.
- Scrimgeour, I. and Close, D., 1999. Regional high-pressure metamorphism during intracratonic deformation: the Petermann Orogeny, central Australia. *Journal of Metamorphic Geology*, 17, 557–572.
- Scrimgeour, I., Close, D. and Edgoose, C.J., 1999. Petermann Ranges 1:250 000 map series: explanatory notes, Northern Territory Geological Survey, Darwin.
- Sprigg, R.C. and Wilson, R.B., 1959. The Musgrave mountain belt in South Australia. *Geological Rundschau*, 47, 531-542.
- Sun, S.-S., Sheraton, J.W., Glikson, A.Y. and Stewart, A.J., 1996. A major magmatic event during 1050–1080 in central Australia and an emplacement age for the Giles Complex. *Australian Geological Survey Organisation Research Newsletter*, 24, 13-15.

- Thomson, B.P., 1976. The Musgrave Block--regional geology. *Economic Geology of Australia and Papua New Guinea*, 1. Metals., Monograph 5. Australasia Institute of Mining and Metallurgy, Melbourne, 451-454 pp.
- Twiss, R.J. and Moores, E.M., 1992. *Structural Geology*. W.H. Freeman and Company, New York, 532 pp.
- Wade, B.P., Barovich, K.M., Hand, M., Scrimgeour, I. and Close, D.F., 2006. Evidence for Early Mesoproterozoic Arc Magmatism in the Musgrave Block, Central Australia: Implications for Proterozoic Crustal Growth and Tectonic Reconstructions of Australia. *Journal of Geology*, 114(1), 43-63.
- Wade, B.P., Hand, M. and Barovich, K.M., 2005. Nd isotopic and geochemical constraints on provenance of sedimentary rocks in the eastern Officer Basin, Australia: implications for the duration of the intracratonic Petermann Orogeny. *Journal of the Geological Society of London*, 162, 513-530.
- White, R.W., Clarke, G.L. and Nelson, D.R., 1999. SHRIMP U-Pb zircon dating of Grenville-age events in the western part of the Musgrave Block, central Australia. *Journal of Metamorphic Geology*, 17, 465-481.
- Williams, I.S., 1998. U-Th-Pb geochronology by ion microprobe. In: M.A. McKibben, W.C. Shanks and W.I. Ridley (Editors), *Applications of microanalytical techniques to understanding mineralizing processes*. *Reviews in Economic Geology*, pp. 1-35.

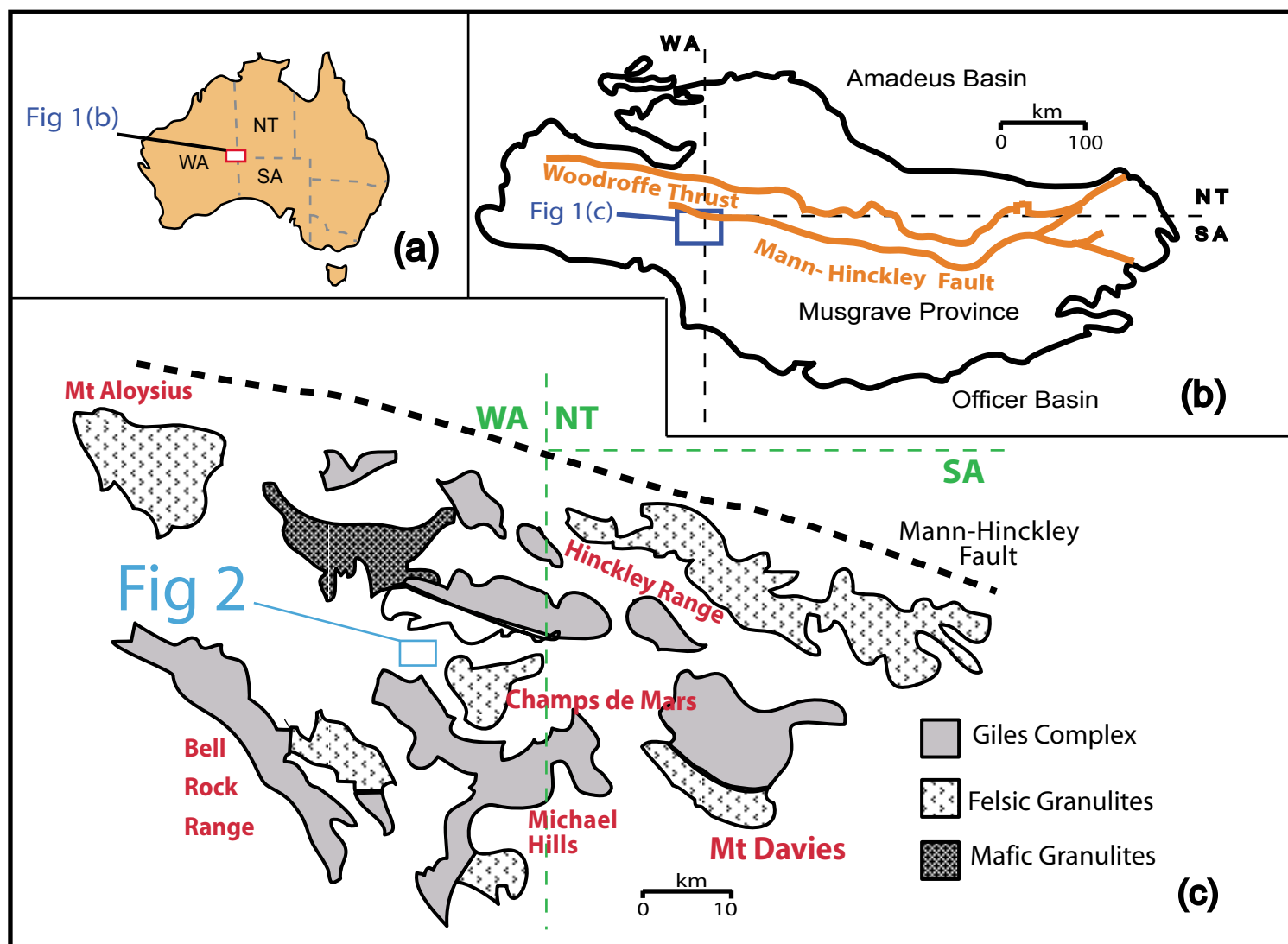
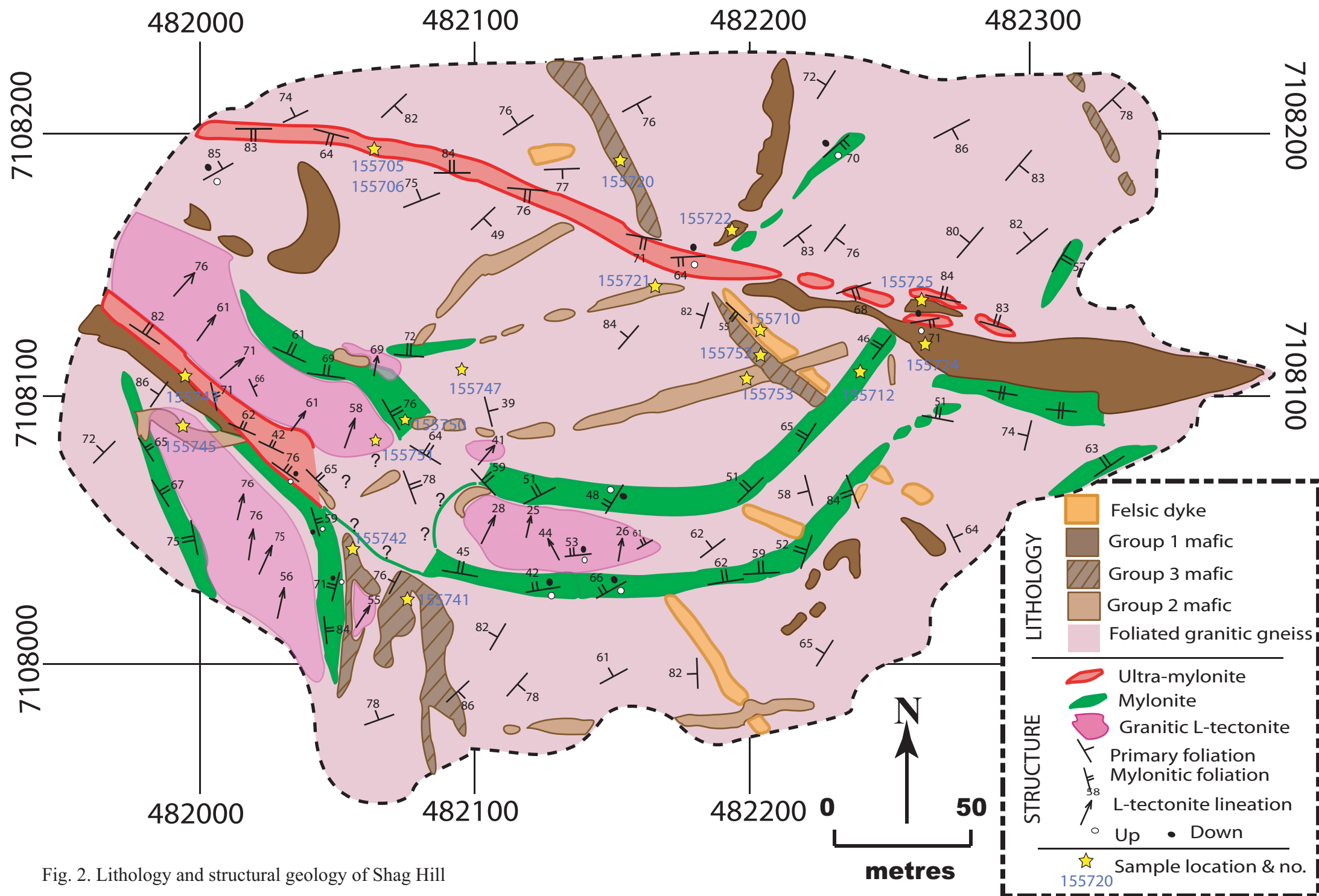
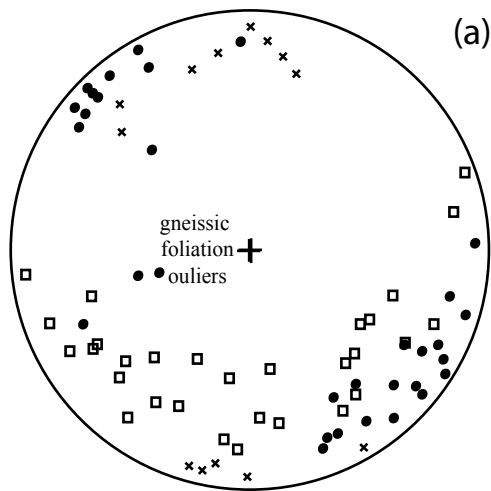
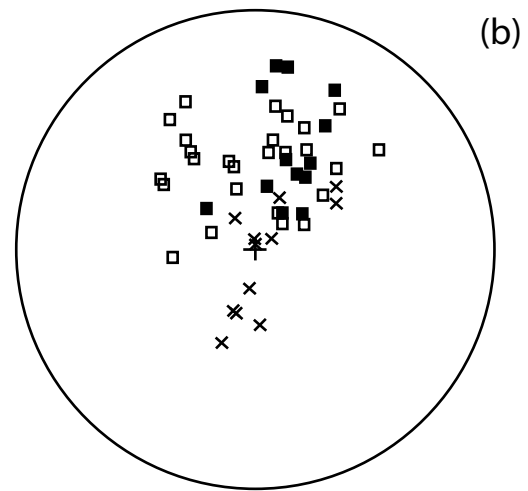


Fig. 1. Geological map of the Musgrave Block, with particular reference to the western Musgrave Block (modified from White *et al.* (1999)). Approximate position of figure 2 is shown in 1 (c).





× = ultramylonite; (n=13), pole to foliation planes
 □ = mylonite ; (n=30), pole to foliation planes
 • = granitic gneiss; (n=32), pole to foliation planes



× = ultramylonitic lineation; (n=14)
 □ = mylonitic lineation; (n=25)
 ■ = L-tectonic lineation; (n=13)

Fig. 3. Stereographic projection of (a) poles to foliation planes and (b) lineations. L-tectonite not included in (a) as it possesses no foliation; granitic gneiss not included in (b) as mineral lineations are poorly developed, at best. Note, outliers in gneissic foliation due to transposition of foliation into younger high strain zones (see text).

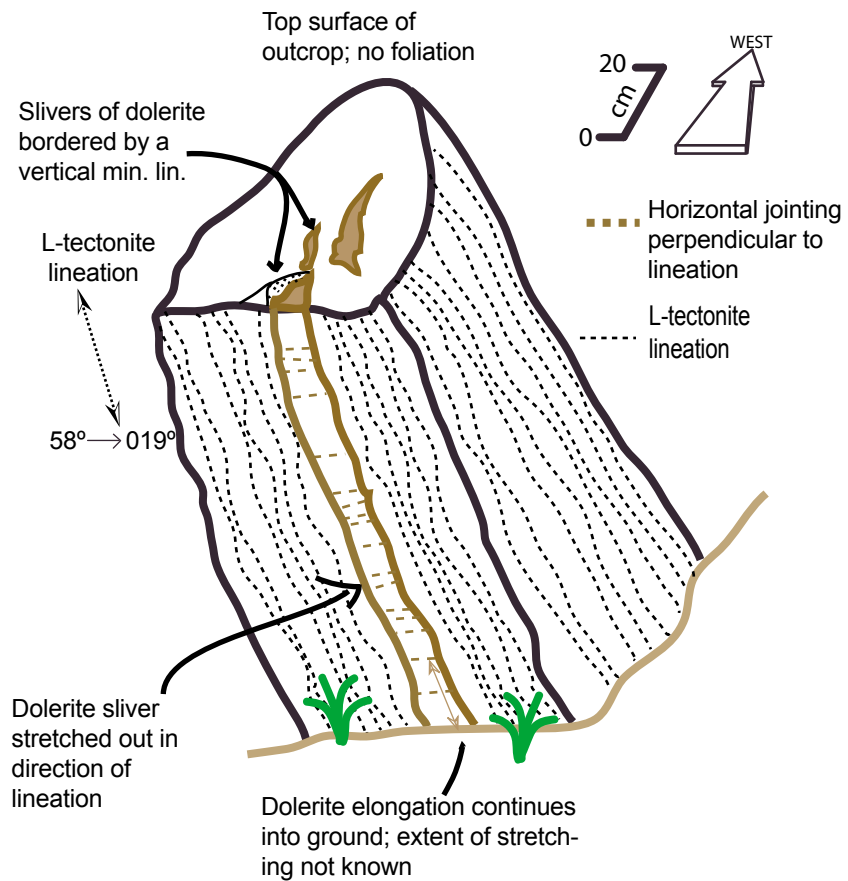


Fig. 4. Schematic diagram describing the observation of lineation-rimmed slivers of mafic material contained within L-tectonic and SL-tectonic granitic gneiss. The horizontal jointing perpendicular to the well-developed mineral stretching lineation suggests that the mafic material has stretched along the mineral lineation within the shear zone.

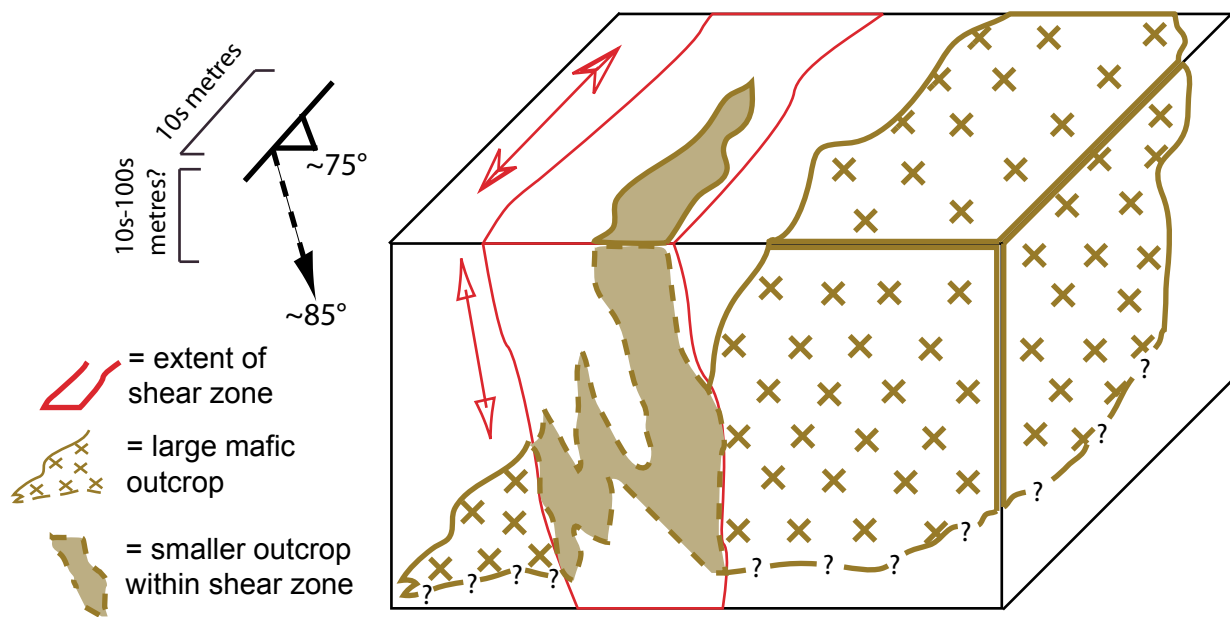


Fig. 5. Schematic diagram describing the occurrence of metre-scale, lineation-rimmed, blocks of mafic material with shear zones. The large blocks, as opposed to cm-scale slivers (Fig. 4), occur adjacent to larger outcrops of identical lithology. The inference is that the extension of the large outcrop at depth is stretched along the mineral lineation within the shear zone. Figure not drawn to scale.

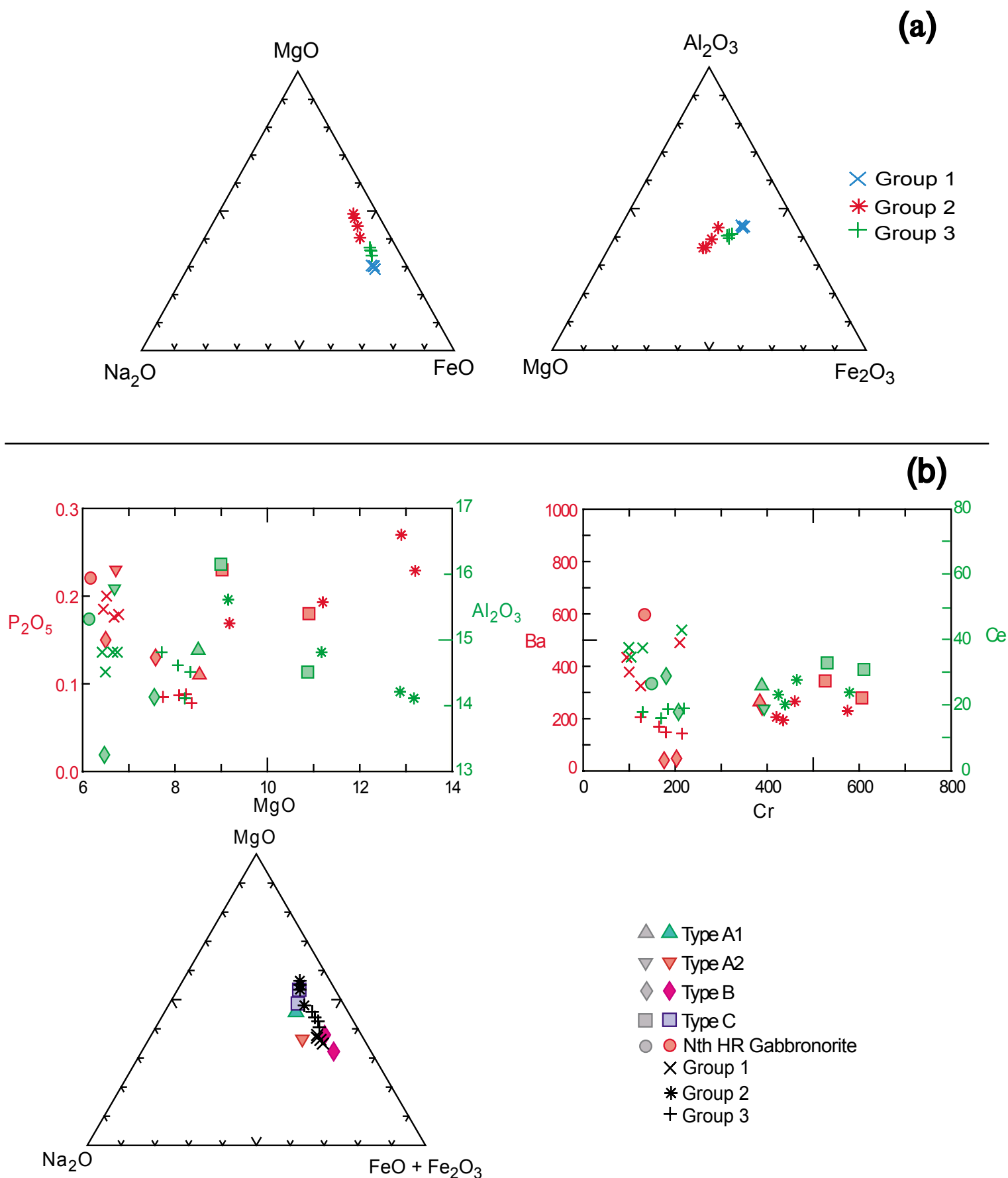


Fig. 6. Plots of various geochemical parameters of (a) mafic outcrops of Shag Hill, and (b) their comparison with previously reported mafic suites. (a) shows the outcrops of Shag Hill falling into three distinct groupings, groups 1-3. (b) shows that group 1 correlates with Nth HR gabbro, group 2 correlates with type C, and type 3 correlates with group B. Note the heterogeneity in type C/group 1 samples, and also the similarity in some respects of type A1/A2 to type C/group 2. Nth HR= northern Hinckley Range; types A1, A2, B & C, and Nth HR gabbro as reported by Glikson et al. (1996).

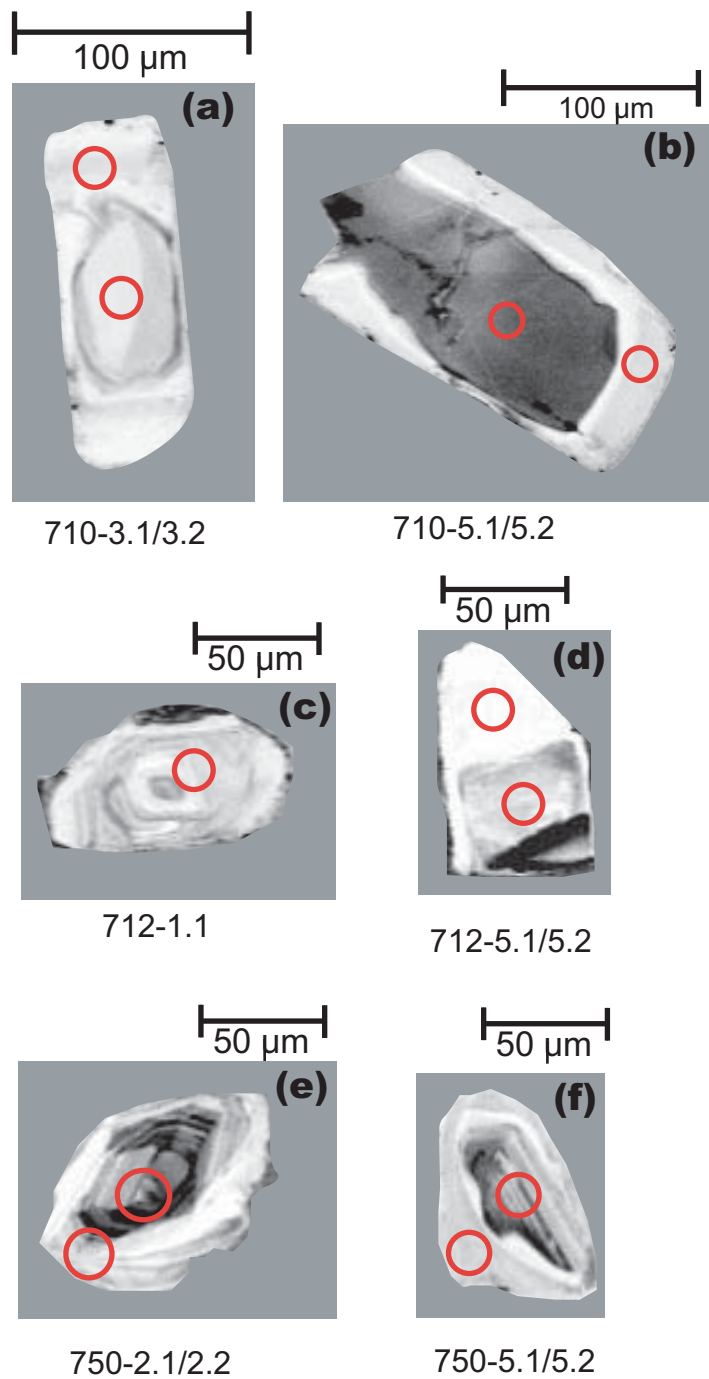


Fig. 7. CL images showing zircon morphology and internal zonation. 710 (a & b) come from sample 155710 (felsic dyke), 712 (c & d) represent sample 155712 (mylonite) and 750 (e & f) represent sample 155750 (mylonite). Red circles show location of SHRIMP spots, and are approximately 20 μm diameter.

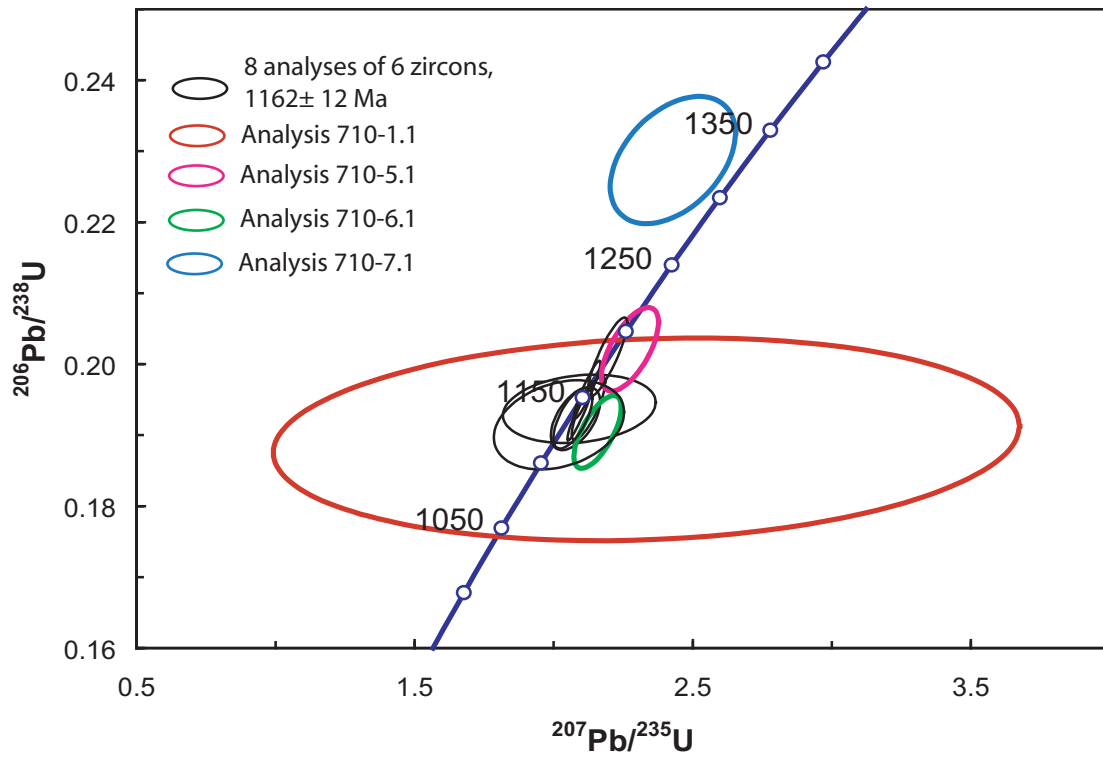


Fig. 8. Concordia plot for sample 155710. Analysis 710-5.1 is from a xenocrystic crystal and is not included in age calculations. Analyses 1.1, 6.1 and 7.1 are significantly discordant and are not used in age calculations (see text).

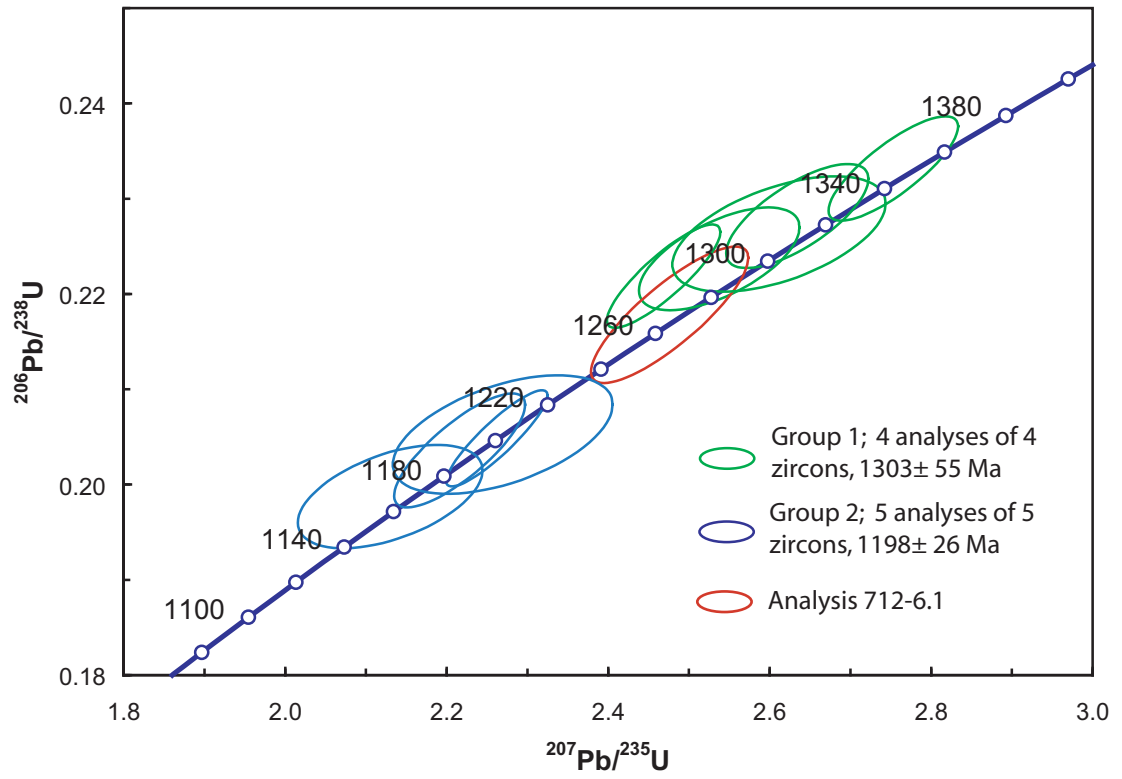


Fig. 9. Concordia plot for sample 155712. Group 1 analyses come from euhedral oscillatory zoned zircon. Group 2 analyses come from featureless-CL zircon rims. Analysis 712-6.1 is not included in age calculations (see text).

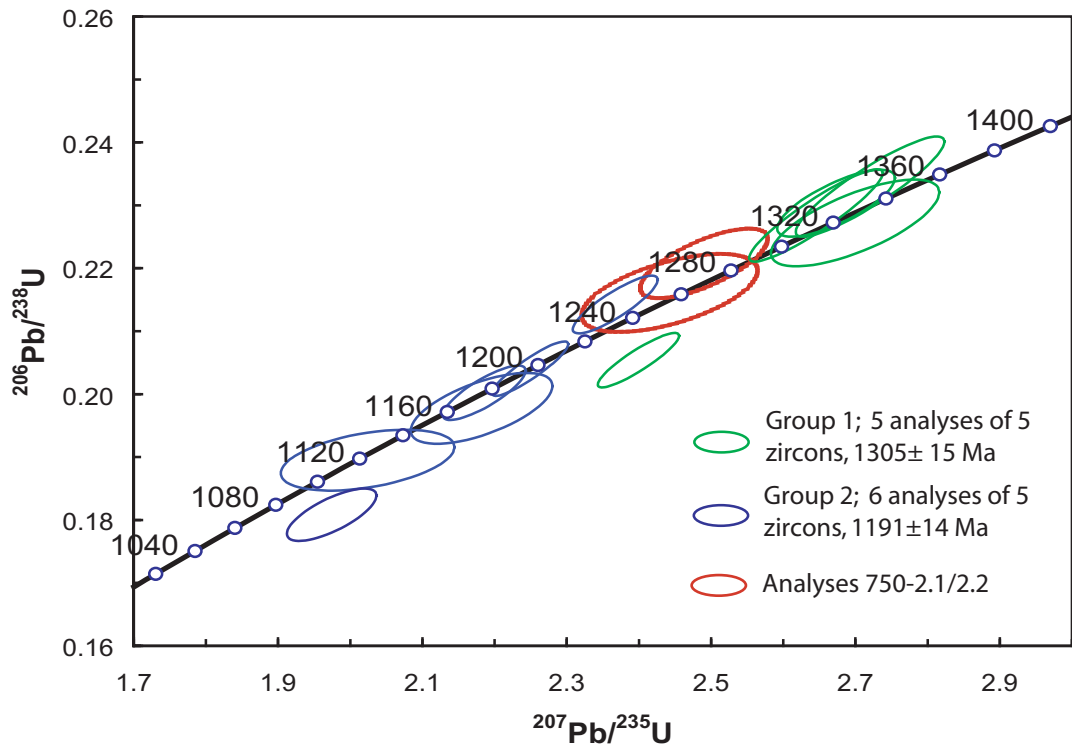


Fig. 10. Concordia plot for sample 155750. Group 1 analyses come from euhedral oscillatory zoned zircon. Group 2 analyses come from featureless-CL zircon rims. Analyses 750-2.1/2.2 are not included in age calculations (see text).

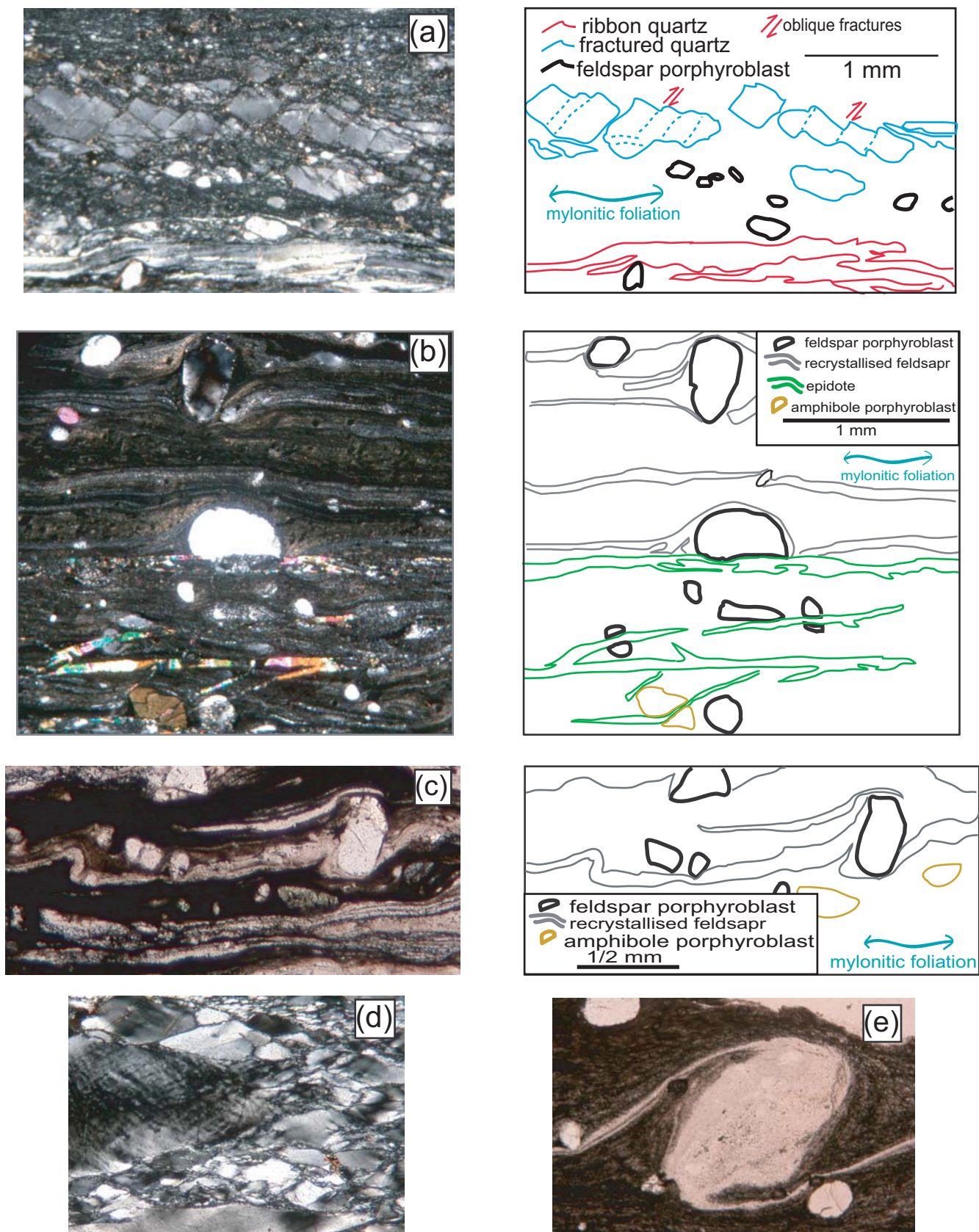


Fig. 11. Microstructural features associated with mylonites and ultramylonites of Shag Hill. All micrographs with crossed polarisers (except (c) & (e)) and all have mylonitic foliation parallel to base of micrograph. All kinematics have dextral shear sense. (a) 155712; displacement of feldspar crystals along fractures inclined to mylonitic foliation. Quartz forms ribbons parallel to foliation. (b) 155705; epidote exists as fracture fill, which cuts across both the mylonitic foliation and porphyroblasts. (c) 155712; recrystallised feldspar warping around feldspar porphyroblast and also forming asymmetric fold. (d) 155750; feldspar in SL- and L-tectonites occurs either as large porphyroblasts (large strained grain to left), diamond shaped crystals (smaller grains, surround porphyroblast), or as fracture fill in the conjugate fracture sets that produce the diamond grains. (e) 155712; asymmetric δ -porphyroblast. Smaller feldspar porphyroblasts also present (top left & bottom right), but show no asymmetry.

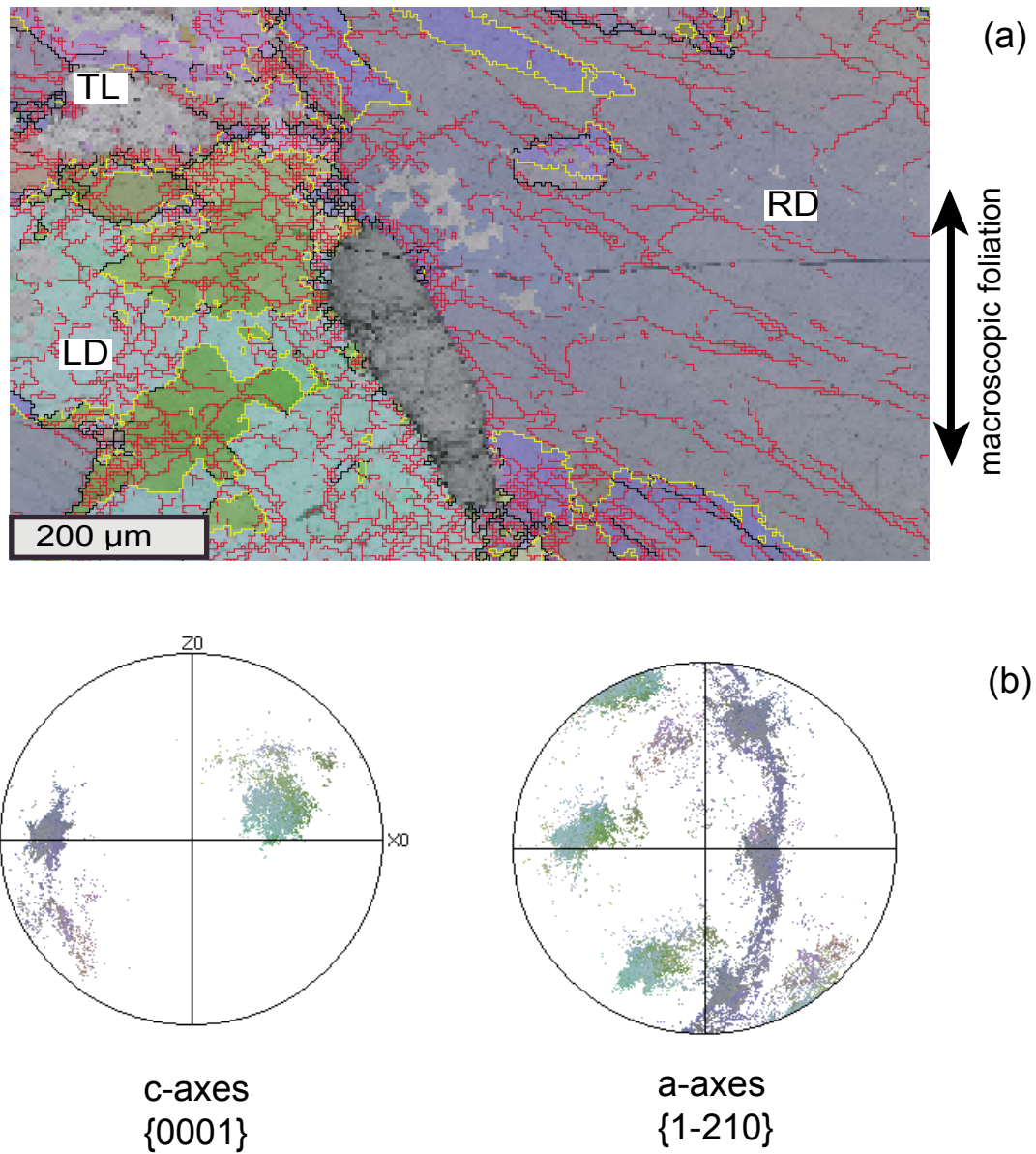


Fig. 12. (a) Automated EBSD map of sample 155747 (Map747); Each pixel (c.44,000) represents a single orientation analysis. Red and black lines represent boundaries between adjacent analyses with $>2^\circ$ and $>10^\circ$ misorientation, respectively. Yellow lines represent Dauphiné twin boundaries. Different colours reflect variation in crystal orientation based on three Euler angles (see Prior et al., 1999), whereas grey pixels represent feldspar or zero indexing. LD, left domain; RD, right domain; TL, top-left domain. (b) Lower hemisphere, equal-area projections of c-axis and a-axis orientation data for the whole data set. The strong grouping (in two orientations) of the c-axis data is due to the fact that only 3 grains have been analysed. The data show that right and top-left domains are essentially equivalent.

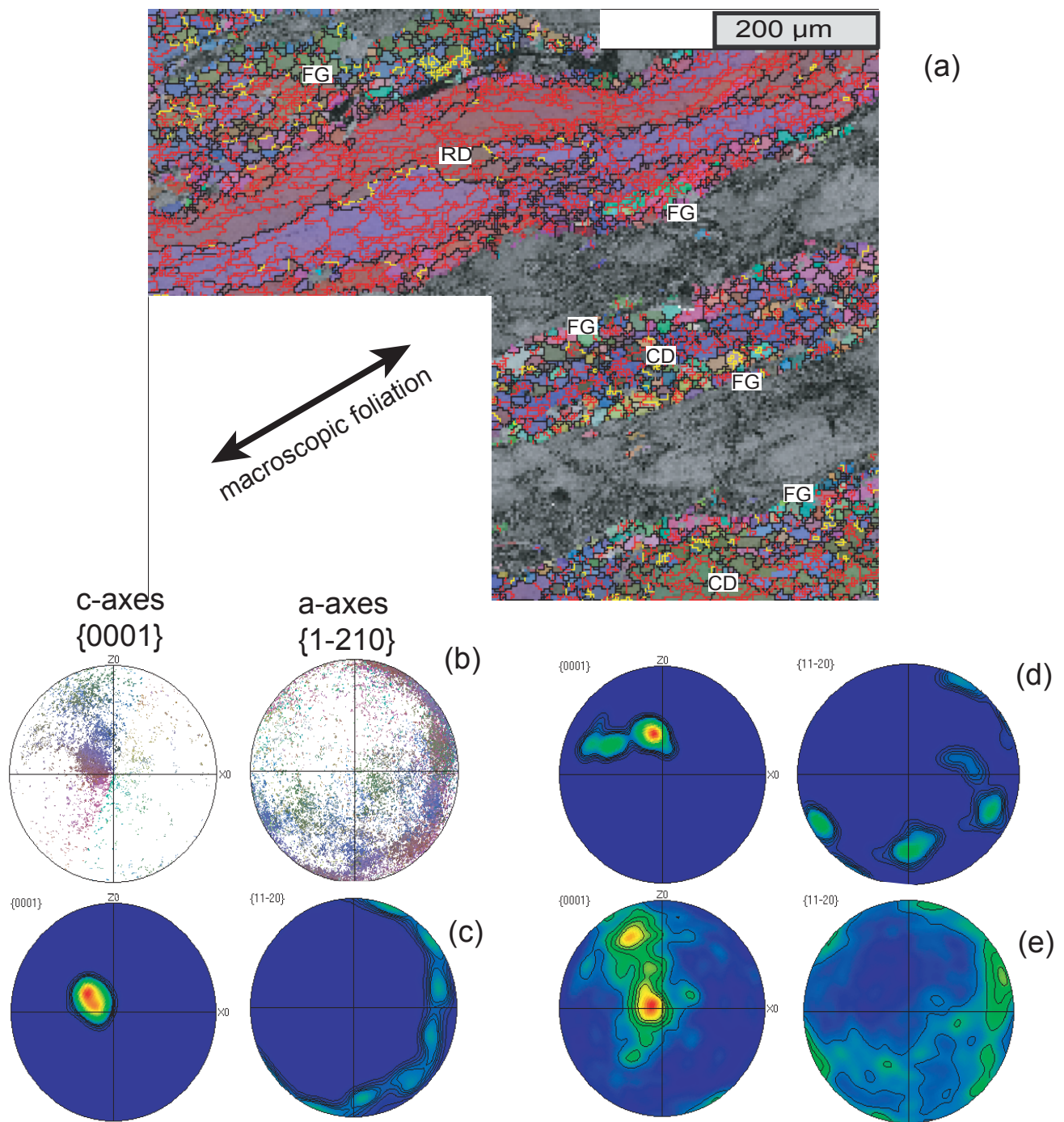


Fig. 13. (a) Map750, a stitch of two automated EBSD maps of sample 155750; Red, black and yellow lines represent $>2^\circ$ misorientation, $>10^\circ$ misorientation and Dauphiné twin boundaries, respectively. Different colours reflect variation in crystal orientation based on three Euler angles (see Prior et al., 1999), grey pixels represent the indexing of feldspar, biotite or zero indexing. RD, ribbon domain; FG, fine grain domain; CD, centre domain. (b) c-axis and a-axis orientation data for the whole data set. (c) Contoured c-axis and a-axis orientation data for the ribbon domain. c-axes concentrated parallel to macroscopic foliation, perpendicular to macroscopic mineral lineation. (d) Contoured c-axis and a-axis orientation data for the centre domain. Orientation essentially equivalent to ribbon domain. (e) Contoured c-axis and a-axis orientation data for the fine grain domain. Both c- and a-axis orientations concentrate asymmetrically as a response to non-coaxial, sinistral, shearing.

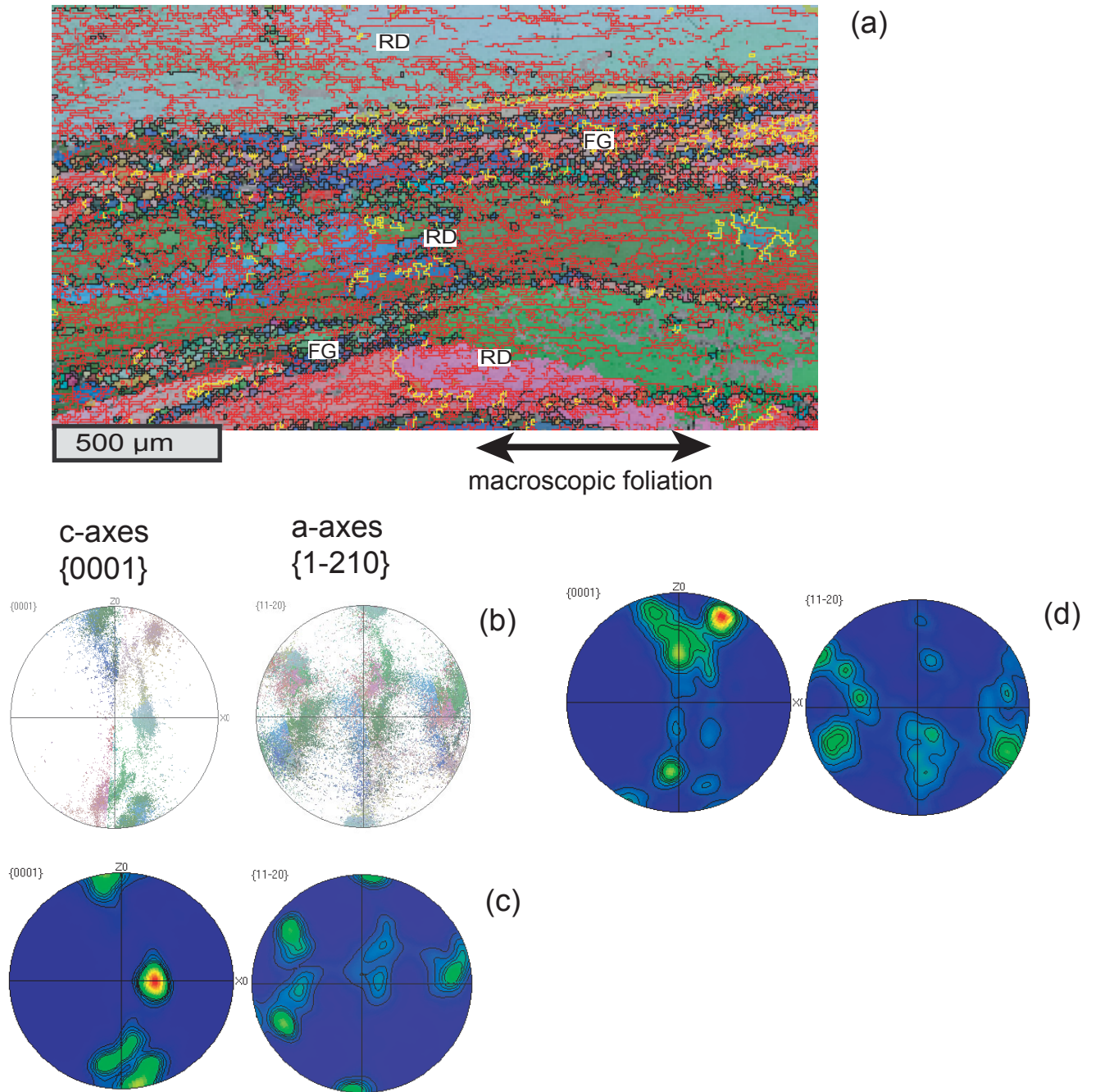


Fig. 14. (a) Map751, a stitch of two automated EBSD maps of sample 155751; Red, black and yellow lines represent $>2^\circ$ misorientation, $>10^\circ$ misorientation and Dauphiné twin boundaries, respectively. Different colours reflect variation in crystal orientation based on three Euler angles (see Prior et al., 1999), grey pixels represent the indexing of feldspar, biotite or zero indexing. RD, ribbon domain; FG, fine grain domain. (b) c-axis and a-axis orientation data for the whole data set. (c) Contoured c-axis and a-axis orientation data for the ribbon domain. The data comes from 4 or 5 different grains (each with $<10^\circ$ misorientation, by definition), and thus essentially comprises 4 or 5 different data points, and cannot be used to produce any definitive conclusions. The data does, however, roughly align with the well-defined patterns of (d). (d) Contoured c-axis and a-axis orientation data for the fine grain domain. The data comprises a cleft girdle pattern orientated about the Z0-axis (c-axis data) and X0-axis (a-axis data), implying simple (coaxial) extension parallel to the macroscopic mineral elongation lineation.

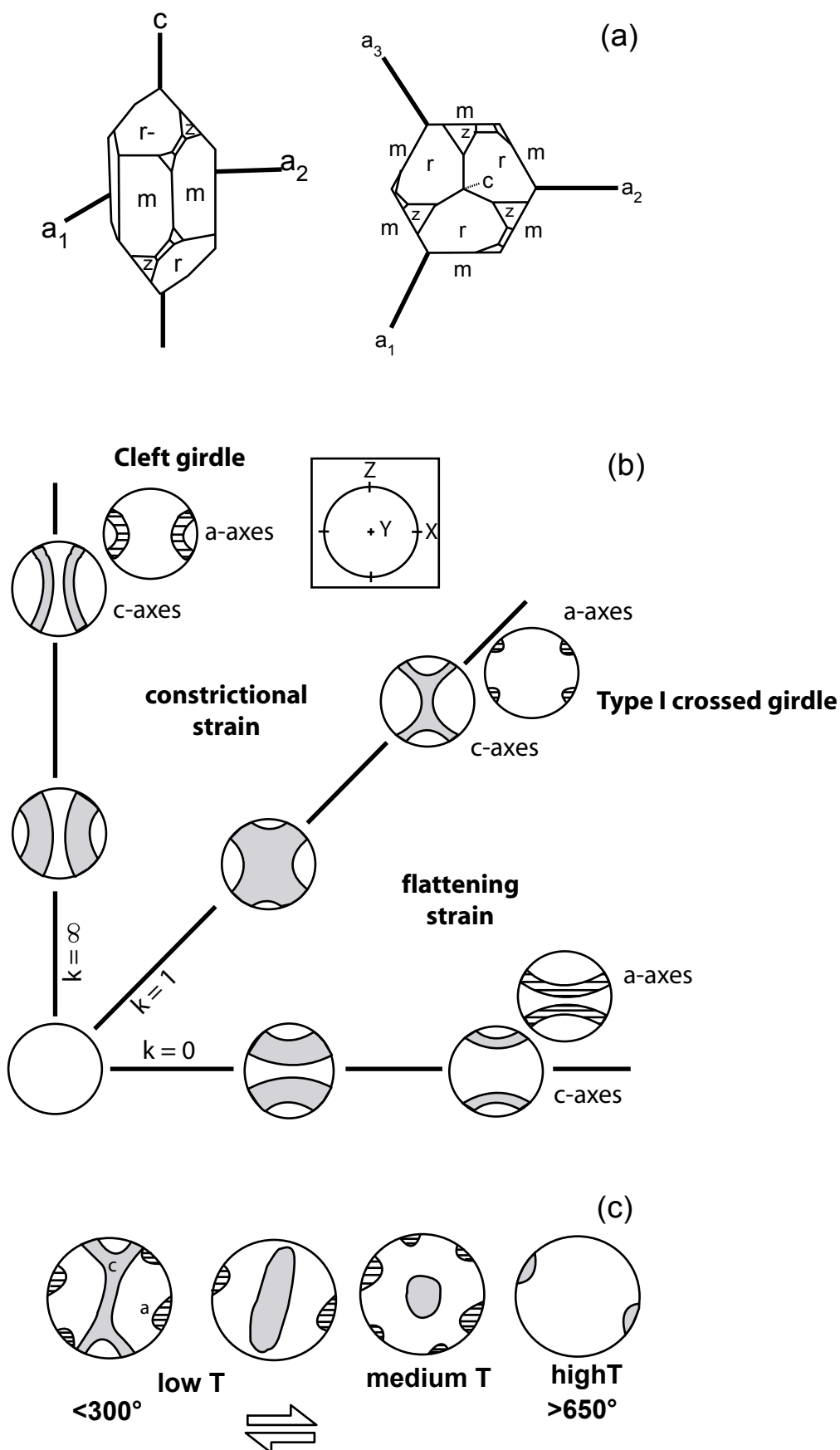


Fig. 15. (a) Schematic crystal diagram showing crystal faces and directions in quartz. (b) Flinn diagram showing c-axis (grey shading) and a-axis (horizontal lines) pole figure patterns for quartz during different coaxial strain geometries. Inset diagram shows the positions of the X-, Y- and Z-axes of the finite strain ellipsoid, with respect to the sample foliation, within the pole figures. (c) Pole figures showing the c-axis (grey shading) and a-axis (horizontal lines) patterns for quartz developing during non-coaxial progressive strain with increasing metamorphic conditions. (a) adapted from *Twiss and Moores (1992)*; (b) & (c) adapted from *Passchier and Trouw (1998)*.

Table 1. Geochemical analysis data

Sample no.	155720	155721	155722	155724	155725	155739	155741	155742
Description	NE-SW trending, planar	NW-SE trending, planar	roughly N-S trending, irregular	roughly E-W trend, irregular	mylonitised outcrop of 177724	NW-SE trending, planar	folded? NE-SW outcrop	folded? NE-SW outcrop
Group	3	2	1	1	1	2	3	3
SiO ₂	50	48.6	49.6	49.7	50.2	46.9	49.8	49.5
Al ₂ O ₃	14.1	15.6	14.8	14.8	14.8	14.1	14.6	14.8
CaO	10.8	10.7	10.2	10.5	10.5	9.72	11	11.1
FeO	9.09	7.68	8.78	9.64	9.39	8.09	8.36	9.24
Fe ₂ O ₃	12.7	11.3	13.3	13.3	13.1	11.7	12.6	12.9
K ₂ O	0.49	0.51	0.84	0.78	0.76	0.46	0.46	0.45
MgO	8.24	9.18	6.78	6.45	6.68	13.2	8.09	7.74
Na ₂ O	2.02	2.25	2.34	2.37	2.39	2.08	1.98	2.13
P ₂ O ₅	0.088	0.169	0.179	0.185	0.176	0.229	0.087	0.085
TiO ₂	0.92	0.95	1.25	1.17	1.12	0.95	0.92	0.93
MnO	0.2	0.18	0.2	0.2	0.2	0.19	0.2	0.2
LOI1000	-0.07	0.08	0.15	-0.03	-0.2	0	-0.02	-0.09
Total	108.58	107.20	108.42	109.07	109.12	107.62	108.08	108.99
Ba	143	206	325	434	378	230	148	206
Be	0.4	0.4	0.7	0.7	0.6	0.5	0.5	0.4
Bi	-0.1	-0.1	-0.1	-0.1	-0.1	-0.1	-0.1	-0.1
Cd	-0.5	-0.5	-0.5	-0.5	-0.5	-0.5	-0.5	-0.5
Ce	19.1	23.3	37.6	37.7	34.8	24	18.9	18
Cr	215	420	125	95	100	575	180	125
Cs	0.1	-0.1	0.2	-0.1	-0.1	-0.1	0.1	0.1
Cu	128	115	151	131	132	124	126	132
Dy	3.75	4.25	5.2	5.35	4.9	3.65	3.65	3.7
Er	2.1	2.55	3	3.2	2.9	2.15	2.2	2.15
Eu	0.95	1.1	1.45	1.45	1.3	1.1	0.95	0.95
Ga	16.6	16.4	18.4	19.4	18.2	13.6	16.2	16.8
Gd	3.4	4	5.2	5.2	4.8	3.4	3.4	3.4
Hf	0.64	1.52	1.56	0.48	0.38	1.34	0.38	0.42
Ho	0.78	0.92	1.12	1.14	1.04	0.78	0.76	0.78
La	8.6	10.2	16.9	16.7	15.9	10.7	8.3	8
Lu	0.3	0.34	0.44	0.42	0.38	0.28	0.28	0.3
Mo	-0.5	-0.5	0.5	-0.5	-0.5	-0.5	-0.5	-0.5
Nb	3	3	6	5	4.5	3	3	3
Nd	10	12.5	19	19.7	18.5	13.6	9.4	9.3
Ni	194	222	164	130	132	468	190	186
Pb	5	5	10	8	10	5	4	6
Pr	2.48	2.98	4.64	4.66	4.26	3.04	2.42	2.38
Rb	14.4	13.6	22.8	18.4	17.6	10.2	12.2	12
Sb	-0.2	-0.2	0.4	-0.2	-0.2	-0.2	-0.2	-0.2
Sc	38	38	32	36	36	36	38	36
Sm	2.8	3.25	4.5	4.75	4.3	3.05	2.85	2.7
Sr	136	160	193	200	183	183	139	146
Ta	0.3	0.3	0.8	0.3	0.3	0.3	0.2	0.2
Tb	0.58	0.68	0.86	0.88	0.8	0.6	0.58	0.6
Th	2.3	1	3.1	0.4	0.5	0.8	1.6	1.6
U	0.2	0.1	0.3	-0.1	-0.1	-0.1	0.2	0.1
V	292	234	294	304	286	200	294	302
Y	20.2	22.6	26.9	28.3	26	19.1	19.2	19.6
Yb	2.05	2.3	2.7	2.85	2.75	1.9	1.9	2.05
Zn	94	76	104	102	110	70	82	90
Zr	12	46	24	7	6	42	6	10

Sample no.	155743	155745	155752	155753
Description	<i>roughly SE trend, irregular</i>	<i>NW-SE trending, planar</i>	<i>NE-SW trending, planar</i>	<i>NW-SE trending, planar</i>
Group	1	2	3	2
SiO2	51.4	47.5	49.8	46.7
Al2O3	14.5	14.8	14.5	14.2
CaO	9.49	10.2	11.1	9.36
FeO	8.74	7.59	7.97	8.29
Fe2O3	12.5	11.8	12.4	12.1
K2O	1.22	0.46	0.41	0.48
MgO	6.52	11.2	8.36	12.9
Na2O	2.4	2.17	1.93	2.23
P2O5	0.2	0.193	0.078	0.27
TiO2	1.18	0.92	0.86	1.11
MnO	0.19	0.19	0.2	0.19
LOI1000	-0.05	0.06	0.08	0.03
Total	108.29	107.08	107.69	107.86
Ba	490	194	169	266
Be	0.7	0.4	0.4	0.4
Bi	-0.1	-0.1	-0.1	-0.1
Cd	-0.5	-0.5	-0.5	-0.5
Ce	43	20.3	16.1	27.8
Cr	210	435	165	460
Cs	-0.1	-0.1	-0.1	-0.1
Cu	118	111	88	94
Dy	5.5	3.65	3.5	4.1
Er	3.05	2.25	2.05	2.4
Eu	1.5	1	0.9	1.2
Ga	18.6	13.2	16.2	14.2
Gd	5.4	3.4	3.2	4
Hf	0.42	1.16	0.6	1.34
Ho	1.1	0.8	0.72	0.84
La	19.8	9.1	7.1	12.3
Lu	0.42	0.3	0.28	0.3
Mo	-0.5	-0.5	-0.5	0.5
Nb	5.5	2.5	3	4
Nd	22.2	11.4	8.9	15
Ni	152	312	190	436
Pb	10	5	5	4
Pr	5.24	2.58	2.08	3.54
Rb	32.8	10.2	11	10.8
Sb	-0.2	-0.2	-0.2	-0.2
Sc	32	34	40	34
Sm	5	2.7	2.4	3.4
Sr	198	155	141	186
Ta	0.3	0.2	0.2	0.3
Tb	0.88	0.56	0.54	0.66
Th	0.8	0.6	1.3	0.9
U	-0.1	-0.1	0.1	0.1
V	264	208	290	216
Y	28.4	19.5	18.5	21.8
Yb	2.85	2	1.9	2.1
Zn	100	60	90	72
Zr	6	33	11	48

Analysis	U ppm	Th ppm	Th/U	% comm 206	% Discordant	Apparent age (Ma)			
						$^{206}\text{Pb}/^{238}\text{U} \pm$		$^{207}\text{Pb}/^{206}\text{Pb} \pm$	
710-1.1	30	34	1.159	5.652	26	1118	32	1412	446
710-2.1	1742	136	0.078	0.072	2	1139	9	1163	6
710-2.2	1559	128	0.082	-0.028	-2	1156	9	1155	7
710-3.1	443	191	0.430	1.121	0	1141	11	1155	105
710-3.2	398	143	0.358	0.189	1	1142	10	1185	13
710-4.1	388	72	0.186	0.975	4	1134	10	1156	29
710-5.1	96	116	1.203	0.261	2	1187	13	1237	27
710-5.2	376	129	0.342	-0.058	4	1181	12	1176	13
710-6.1	141	150	1.059	0.489	0	1124	11	1250	23
710-7.1	515	451	0.876	-0.094	11	1328	19	1121	69
710-8.1	514	132	0.256	0.471	-16	1134	9	1147	21
710-9.1	74	140	1.900	0.696	1	1129	14	1108	91

Table 2. Zircon analyses from sample 155710.

Analysis	Group	U ppm	Th ppm	Th/U	% comm 206	% Discordant	Apparent age (Ma)			
							$^{206}\text{Pb}/^{238}\text{U} \pm$		$^{207}\text{Pb}/^{206}\text{Pb} \pm$	
712-1.1	2	313	183	0.583	-0.045	-3	1195	13	1171	18
712-2.1	2	118	259	2.187	-0.026	-3	1169	12	1140	38
712-3.1	1	310	250	0.806	-0.122	-3	1351	12	1330	14
712-4.1	1	215	125	0.580	-0.148	-5	1301	12	1252	25
712-5.1	2	565	71	0.126	-0.052	-1	1201	11	1199	10
712-5.2	1	232	136	0.586	-0.056	-4	1325	12	1286	19
712-6.1	1	279	162	0.579	0.054	-2	1270	15	1256	17
712-7.1	2	433	98	0.227	-0.420	-7	1292	12	1214	12
712-8.1	2	79	243	3.077	0.085	-1	1203	14	1202	42
712-8.2	1	134	59	0.444	0.185	-3	1315	13	1286	34

Table 3. Zircon analyses from sample 155712.

Analysis	Group	U ppm	Th ppm	Th/U	% comm 206	% Discordant	Apparent age (Ma)			
							$^{206}\text{Pb}/^{238}\text{U} \pm$		$^{207}\text{Pb}/^{206}\text{Pb} \pm$	
750-1.1	2	201	294	1.466	0.367	1	1119	11	1133	44
750-1.2	2	385	664	1.724	0.200	10	1072	9	1176	17
750-2.1	1	119	194	1.635	0.248	-1	1261	13	1245	33
750-2.2	2	192	160	0.834	0.115	-3	1286	12	1241	20
750-3.1	1	1548	685	0.442	0.221	9	1204	9	1309	8
750-4.1	2	993	128	0.129	0.024	0	1197	9	1196	8
750-5.1	1	78	101	1.299	0.000	2	1320	15	1342	24
750-5.2	2	117	268	2.284	0.106	3	1163	12	1198	28
750-6.1	1	301	263	0.876	0.190	-3	1336	11	1297	16
750-7.1	2	732	833	1.137	0.085	0	1176	9	1177	12
750-8.1	2	740	217	0.293	0.030	-4	1251	10	1200	10
750-9.1	1	269	188	0.698	0.028	-3	1350	17	1308	13
750-10.1	1	574	61	0.107	0.085	-3	1326	16	1293	11

Table 4. Zircon analyses from sample 155750.

This Record is published in digital format (PDF) and is available online at:
www.dmp.wa.gov.au/GSWApublications.
Laser-printed copies can be ordered from the Information Centre for the
cost of printing and binding.

Further details of geological publications and maps produced by the
Geological Survey of Western Australia can be obtained by contacting:

Information Centre
Department of Mines and Petroleum
100 Plain Street
EAST PERTH, WESTERN AUSTRALIA 6004
Phone: (08) 9222 3459 Fax: (08) 9222 3444
www.dmp.wa.gov.au/GSWApublications

